Check for updates

JGR Earth Surface

RESEARCH ARTICLE
10.1029/2023JF007588

Radar-Derived Crystal Orientation Fabric Suggests Dynamic Stability at the Summit of Hercules Dome

B. H. Hills[1,2], N. Holschuh[3], A. O. Hoffman[4], A. N. Horlings[1,5], E. Erwin[6,7], L. R. Kirkpatrick[1], T. J. Fudge[1], E. J. Steig[1], and K. Christianson[1]

[1]Department of Earth and Space Sciences, University of Washington, Seattle, WA, USA, [2]Department of Geophysics, Colorado School of Mines, Golden, CO, USA, [3]Department of Geology, Amherst College, Amherst, MA, USA, [4]Lamont-Doherty Earth Observatory, Columbia University, Palisades, NY, USA, [5]Institute for Arctic and Alpine Research, University of Colorado, Boulder, CO, USA, [6]School of Earth and Climate Sciences, University of Maine, Orono, ME, USA, [7]Cold Regions Research and Engineering Laboratory, Hanover, NH, USA

Key Points:

- We constrain present and past ice dynamics at Hercules Dome, East Antarctica, using measurements of ice flow and crystal orientation fabric (COF)
- We find evidence of divide flow in both vertical velocities and COF, particularly at the summit of Hercules Dome
- Models of COF suggest that divide orientation, position, and shape have been dynamically stable since at least 5 ka

Supporting Information:

Supporting Information may be found in the online version of this article.

Correspondence to:

B. H. Hills,
benjamin.hills@mines.edu

Citation:

Hills, B. H., Holschuh, N., Hoffman, A. O., Horlings, A. N., Erwin, E., Kirkpatrick, L. R., et al. (2025). Radar-derived crystal orientation fabric suggests dynamic stability at the summit of Hercules Dome. *Journal of Geophysical Research: Earth Surface*, *130*, e2023JF007588. https://doi.org/10.1029/2023JF007588

Received 8 DEC 2023
Accepted 21 JAN 2025

Author Contributions:

Conceptualization: B. H. Hills, N. Holschuh, K. Christianson
Data curation: B. H. Hills, L. R. Kirkpatrick, T. J. Fudge, K. Christianson
Formal analysis: B. H. Hills
Funding acquisition: T. J. Fudge, E. J. Steig, K. Christianson
Investigation: B. H. Hills, N. Holschuh, A. O. Hoffman, A. N. Horlings, E. Erwin, L. R. Kirkpatrick, T. J. Fudge, E. J. Steig, K. Christianson
Methodology: B. H. Hills, N. Holschuh, A. O. Hoffman, A. N. Horlings, T. J. Fudge, K. Christianson
Project administration: T. J. Fudge, E. J. Steig, K. Christianson
Resources: B. H. Hills, N. Holschuh, A. N. Horlings, T. J. Fudge, E. J. Steig, K. Christianson

© 2025. American Geophysical Union. All Rights Reserved.

Abstract Hercules Dome is a prospective ice-core site due to its setting in the bottleneck between East and West Antarctica. If ice from the last interglacial period has been preserved there, it could provide critical insight into the history of the West Antarctic Ice Sheet. The likelihood of a continuous, well-resolved, easily interpretable climate record preserved in ice extracted from Hercules Dome depends in part on the persistence of ice-flow dynamics at the divide. Significant changes in ice drawdown on either side of the divide, toward the Ross or Ronne ice shelves, could change the relative thickness of layers and the deposition environment represented in the core. Here, we use radar sounding to survey the ice flow at Hercules Dome. Repeated radar acquisitions show that vertical velocities are consistent with expectations for an ice divide with a frozen bed. Polarimetric radar acquisitions capture the ice-crystal orientation fabric (COF) which develops as ice strains, so it depends on both the pattern of ice flow and the time over which flow has been consistent. We model the timescales for COF evolution, finding that the summit of Hercules Dome has been dynamically stable in its current configuration, at least over the last five thousand years, a time period during which the Antarctic ice sheet was undergoing significant retreat at its margins. The evident stability may result from a prominent bedrock ridge under the divide, which had not been previously surveyed and has therefore not been represented in the bed geometry of coarsely resolved ice-sheet models.

Plain Language Summary Hercules Dome is a localized high point in the ice surface between East and West Antarctica. Based on present-day flow patterns highlighted in prior work, there is reason to believe that ice from 130 thousand years ago may be preserved there. The old ice would give insight on behavior of the West Antarctic Ice Sheet during a prior warm period in Earth's history. However, if the ice flow patterns near Hercules Dome have changed over time, the old ice may not be preserved in a state which can be easily interpreted. To study the ice flow, we use radar measurements of (i) vertical movement, and (ii) crystal orientation. The orientations of crystals change over time as the ice is stretched, so they can reveal information about ice flow and how long it has been consistent. We find that the ice flow at the summit of Hercules Dome has been consistent for at least the last five thousand years, as the Antarctic Ice Sheet shrank coming out of the last ice age. This stability is likely caused by a large ridge of rock beneath the ice, which had not been discovered until now.

1. Introduction

Modeling studies have shown that a hypothetical collapse of the West Antarctic Ice Sheet (WAIS) would change the regional atmospheric circulation (Steig et al., 2015), forcing warm air onto the edge of the East Antarctic Plateau. That atmospheric effect would be preserved in the ice at Hercules Dome as positive oxygen isotope anomalies (Dütsch et al., 2023). Therefore, if WAIS collapsed during the last interglacial period, as has been suggested by both genomic evidence (Lau et al., 2023) and some ice-sheet models (DeConto & Pollard, 2016), Hercules Dome would be uniquely situated to preserve the signal of that collapse. Still, the question remains whether the historic ice flow would favor the preservation of a continuous stratigraphy through the ice column in a way that would lead to an interpretable ice core.

Historic ice-dynamic settings at Hercules Dome would have depended, at least in part, on the relative evolution of the two downstream ice shelves, the Ronne and Ross. For example, during the Last Glacial Maximum (LGM),

Software: B. H. Hills
Supervision: N. Holschuh, T. J. Fudge, E. J. Steig, K. Christianson
Validation: B. H. Hills, N. Holschuh, A. O. Hoffman, A. N. Horlings, E. Erwin, T. J. Fudge, E. J. Steig, K. Christianson
Visualization: B. H. Hills, N. Holschuh, A. O. Hoffman, K. Christianson
Writing – original draft: B. H. Hills
Writing – review & editing: B. H. Hills, N. Holschuh, A. O. Hoffman, A. N. Horlings, E. Erwin, L. R. Kirkpatrick, T. J. Fudge, E. J. Steig, K. Christianson

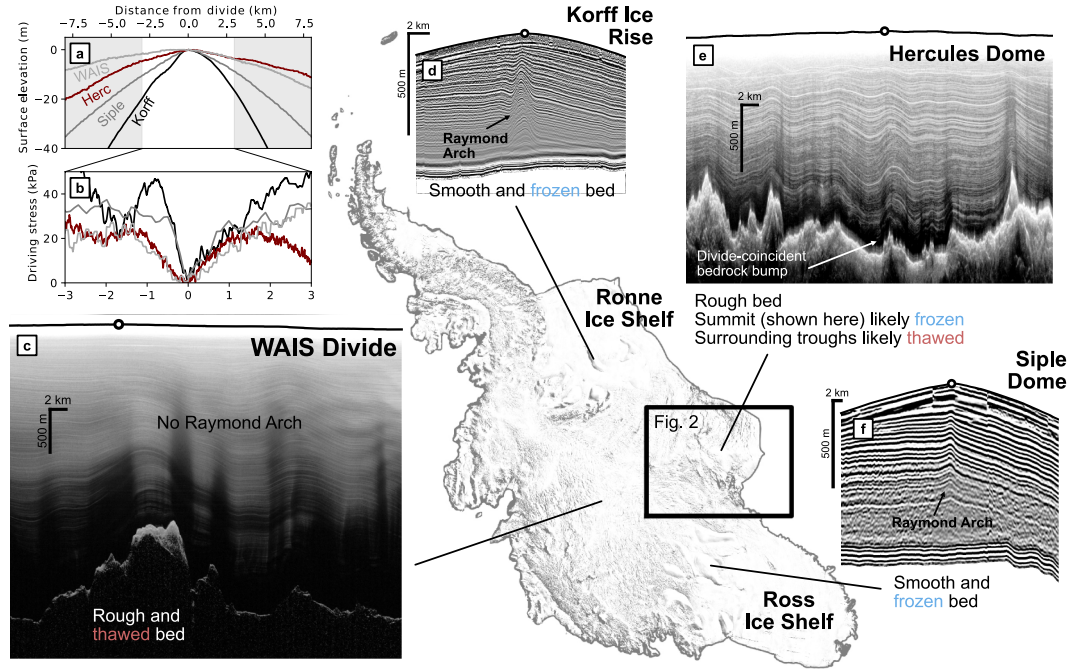

Figure 1. A comparison of ice geometry and radar stratigraphy between Antarctic sites with strong and weak Raymond Effect. The reference map of West Antarctica is on MODIS imagery (Haran et al., 2018). Surface height (a) and driving stress (b) are shown for all four divides in the radar images: (c) West Antarctic Ice Sheet Divide (CReSIS, 2024), (d) Korff Ice Rise (Kingslake et al., 2016), (e) Hercules Dome (pers. comm. Duncan Young/COLDEX project), (f) Siple Dome (Gades et al., 2000).

~20 ka, and through ice-sheet retreat in the Holocene, ice-sheet modeling results show a considerably different ice sheet, with different ice-stream behavior (Albrecht et al., 2020a, 2020b; DeConto & Pollard, 2016; Golledge et al., 2012). If the divide position at Hercules Dome is primarily dependent on downstream effects, then the interplay between the ice shelves may have forced divide migration between them (i.e., at Hercules Dome).

Past investigations have looked for signs of divide stability in imaged radar stratigraphy (Figure 1). A raised arch in the englacial layers is expected to form at the divide position since ice is particularly viscous at the low shear stresses there (Raymond, 1983). Modeling studies have shown that development of such a "Raymond Arch" requires a frozen bed (Pettit et al., 2003) and stable flow over a characteristic timescale (time for accumulation to propagate the full ice thickness) (Martín, Hindmarsh, & Navarro, 2009; Nereson et al., 1998; Pettit & Waddington, 2003). At particularly well-developed divides, a signature crystal orientation fabric (COF) can stiffen the ice further and exaggerate the Raymond Effect (Martín, Gudmundsson, et al., 2009). Observed Raymond Arches have commonly been at coastal domes and ice rises, both of which have relatively thin ice and high accumulation (short characteristic time) (Conway et al., 1999; Vaughan et al., 1999). These features have been notably absent from interior ice divides (e.g., Neumann et al., 2008) even where the Raymond Effect has been directly measured in the present-day vertical velocities (Gillet-Chaulet et al., 2011). Their absence from interior sites is likely due to the longer characteristic time there but could also be due to the smaller driving stress gradient which is dependent on both the surface slope and the ice thickness (Figure 1b).

Hercules Dome forms the interior ice-sheet divide in the region connecting East and West Antarctica, deemed the "bottleneck" (Jacobel et al., 2005) (Figure 2). To the polar-stereographic north (all subsequent cardinal directions are expressed in the same polar-stereographic grid, EPSG:3031), ice flows toward the Ronne Ice Shelf through Foundation Ice Stream. To the south, ice flows toward the Ross Ice Shelf through two drainages, van der Veen Ice Stream (a tributary of Whillans Ice Stream) and Reedy Glacier (a tributary of Mercer Ice Stream). The ice in this area is underlain by deep bedrock troughs and U-shaped valleys which are likely thawed at the bed (Winter et al., 2018). The troughs appear to be fault-bounded and were incised further by streaming ice flow during a time when the ice-sheet geometry was considerably different from today (Hoffman, Holschuh, et al., 2023). Evidence from radar stratigraphy indicates that the troughs and valleys continue to steer ice flow today, limiting drawdown of ice

21699011, 2025, 3, Downloaded from https://agupubs.onlinelibrary.wiley.com/doi/10.1029/2023JF007588 by Benjamin Hills - University Of Washington Lib , Wiley Online Library on [26/02/2025]. See the Terms and Conditions (https://onlinelibrary.wiley.com/terms-and-conditions) on Wiley Online Library for rules of use; OA articles are governed by the applicable Creative Commons License

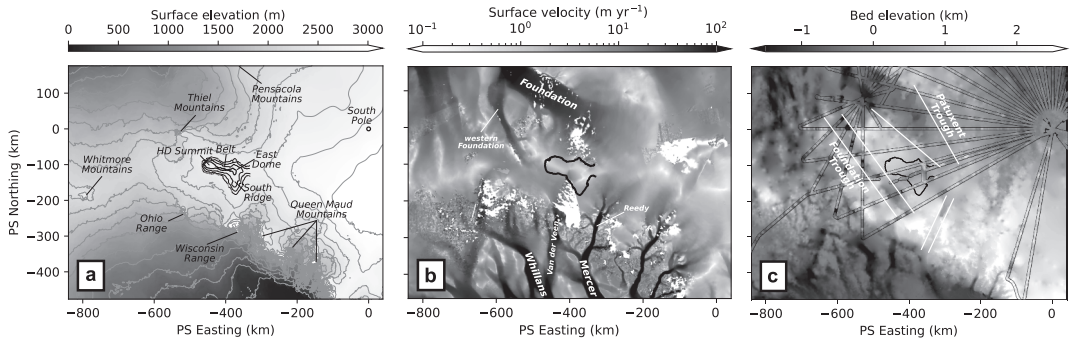

Figure 2. The ice-sheet setting near Hercules Dome. (a) Ice surface elevation from the Reference Elevation Model of Antarctica (Howat et al., 2019). Contour spacing is 200 m away from and 20 m at Hercules Dome. (b) Ice surface velocity from interferometric SAR satellite data products (Mouginot et al., 2019). (c) Bed elevation from BedMachine Antarctica (Morlighem et al., 2020) and prior regional radar surveys (Jacobel et al., 2005; Winter et al., 2018).

from the higher East Antarctic Plateau and possibly influencing ice-sheet divide migration in the region (Hoffman, Holschuh, et al., 2023; Winter et al., 2018).

An initial ground-based geophysical survey of Hercules Dome (Jacobel et al., 2005) focused near an area that was then thought to be the dome summit based on state-of-the art surface topography from that time. Those authors deemed the dome to be an ideal site for an ice core based on their stratigraphic constraints of snow accumulation and ice flow. Subsequent work has obfuscated their initial interpretation of the radar stratigraphy, implying a more complicated ice-flow history for their chosen location on the dome, toward East Antarctica, especially for ice from before the Holocene (Hoffman, Holschuh, et al., 2023). We now know that their false summit ("East Dome") forms the corner of a triple divide, with the prominent north-south flow divide extending to the west in a topographic saddle (which we call the "Belt"), and a secondary divide ("South Ridge") extending to the south toward the Ross Ice Shelf. The true summit of Hercules Dome ("HD Summit") is at the westernmost extent of the primary divide. Divide-like flow has been confirmed at HD Summit within the measured vertical velocities (Fudge et al., 2022). That observation and their thermal modeling result together suggest that the ice-bed interface is likely frozen at this location. Moreover, kinematic models of ice flow suggest that interglacial ice is preserved deep below the summit (Fudge et al., 2022).

Here, we investigate ice-divide dynamics at Hercules Dome, expanding on prior geophysical surveys. Since Raymond Arches have typically not been observed, and may not be expected, at interior ice-sheet divides like this one, we innovate on the geophysical techniques used to assess divide stability. First, we supplement prior constraints on the ice-sheet geometry and dynamics through more complete surveys with radar profiling, radar interferometry, and Global Navigation Satellite System (GNSS). Second, we add novel constraints on the historical ice flow using a radar polarimetry survey and associated interpretations of COF anisotropy. Following the presentation of these newly collected data sets, we use the radar-derived COF results to motivate a series of COF model experiments. We describe and apply a model for COF evolution that we use to understand the history of strain represented in the measured COF signals. We discuss our results, both measured and modeled, within the current understanding of WAIS history during ice-sheet retreat in the Holocene.

2. Geophysical Methods

The data presented here were collected over four separate field seasons between January 2019 and January 2023. Not all sites were visited each year due to the logistical burden during this time period. For instruments requiring repeat acquisitions, the time between visits varies from one to 3 years, depending on the site. Where possible, surveys were aligned with ice flow so that each transect crosses the local ice divide. Along five of those cross-divide transects we used a combination of measurement techniques to survey targeted aspects of the ice geometry and flow, each described in sequence below.

21699011, 2025, 3, Downloaded from https://agupubs.onlinelibrary.wiley.com/doi/10.1029/2023JF007588 by Benjamin Hills - University Of Washington Lib , Wiley Online Library on [26/02/2025]. See the Terms and Conditions (https://onlinelibrary.wiley.com/terms-and-conditions) on Wiley Online Library for rules of use; OA articles are governed by the applicable Creative Commons License

21699011, 2025, 3, Downloaded from https://agupubs.onlinelibrary.wiley.com/doi/10.1029/2023JF007588 by Benjamin Hills - University Of Washington Lib , Wiley Online Library on [26/02/2025]. See the Terms and Conditions (https://onlinelibrary.wiley.com/terms-and-conditions) on Wiley Online Library for rules of use; OA articles are governed by the applicable Creative Commons License

2.1. Global Navigation Satellite System Survey

We surveyed the ice surface using GNSS to geolocate radar profiles, measure surface elevation, and derive in situ measurements of ice-surface velocity. We used Septentrio Altus APS3G as well as Trimble NetR8 and NetRS receivers. For all receivers, we sampled at 1 Hz. We used the Canadian Spatial Reference System precise-point positioning (Tétreault et al., 2005) to convert from raw GNSS files to positions through time.

We collected 1,812 line-km of dual-frequency GNSS data along and between profiling radar lines. For this kinematic profiling, the antennas were mounted on conduit attached to a snowmobile that extended ∼2 m above the snow surface. These data are used for spatial referencing and interpolation of the profiling radar data presented below.

Spaceborne surface velocity measurements are difficult in the ice-sheet interior where ice flow is slow and satellite data coverage is sparse (Mouginot et al., 2019). Thus, we calculate surface velocity measurements by differencing repeat, static GNSS acquisitions. Measurement locations (monuments) were marked using conduit driven ∼20–30 cm into the snow surface. At each location, the GNSS antenna was attached to the monument using a removable mount, and data were collected for at least 10 min. The monument position for each measurement is the mean of all position solutions calculated from the 10-min measurement interval. Uncertainties are calculated as the standard deviation of the position solutions, which is ∼2 cm in the horizontal dimensions. We measured surface velocity at a total of 26 sites laid out along the five intensive survey transects. We calculate along-track strain rates by linear regression of the measured velocities for all sites along a given transect. Since velocities are slow (∼1–10 cm yr^{-1}) relative to the position uncertainty, especially near the ice divide, calculating the strain rate between only a single pair of sites would lead to large uncertainty, so we calculate only a single strain rate per transect by regressing over all velocities in the entire transect.

2.2. Profiling Radar Survey

To constrain the ice geometry, we collected 793 line-km of ground-based profiling radar data with two separate instruments. The first profiling radar instrument was an impulse radar (Welch & Jacobel, 2003) with 3-MHz dipole antennas. We profiled a total of 537 line-km with this instrument. The hardware and processing flow were the same as in previous studies (e.g., Christianson et al., 2016; Hills et al., 2022). Absolute range uncertainty is roughly 1/4 wavelength (∼14 m), while the relative uncertainty from crossover analysis is ∼1 m. The second instrument was a ground-based version of the Multichannel Coherent Radar Depth Sounder (MCoRDS) with which we profiled 256 line-km. This ground-based MCoRDS system had multiple antenna elements, capable of resolving off-nadir scattering for high-resolution cross-track swath mapping (Hoffman, Holschuh, et al., 2023). Data from this instrument were processed using the standard pipeline from Open Polar Radar (2024). The radar profiles and interpreted bed locations presented here are for nadir-focused data only (for a more thorough description of the data processing and off-nadir capabilities see Hoffman, Holschuh, et al. (2023)).

Ice surface elevation and receiver position were measured along each radar profile with a GNSS antenna as explained above. In select locations where the GNSS receiver failed to collect data, surface elevation was extracted from the Reference Elevation Model of Antarctica (REMA) (Howat et al., 2019). Elevation of the bedrock interface is estimated as the surface elevation minus interpreted ice thickness with a correction for firn density using the shallow core drilled within the study area (Steig et al., 2005). We also present interpreted bed positions from three additional profiling radar systems, none of which are the focus of this investigation but provide context for regional ice geometry and flow. The ITASE traverse from Byrd to South Pole Station and directly through Hercules Dome used the same ground-based radar as the first radar instrument above (Jacobel et al., 2005; Welch & Jacobel, 2003). Two airborne surveys have flown directly over Hercules Dome, first with the Polarimetric Airborne System Instrument as a part of the broader PolarGap survey (Winter et al., 2018) and second with the Multifrequency Airborne Radar-sounder for Full-phase Assessment as a part of the surveying done in January 2023 for the Center for Oldest Ice Exploration. For each, we use bed elevations provided by the data owners in our interpretation here.

2.3. Phase-Sensitive Radar Survey

To constrain the past and present ice flow, we acquired Autonomous phase-sensitive Radio Echo Sounding (ApRES) (Nicholls et al., 2015) data at 36 sites. At each site, the antennas were placed ∼10 m apart, oriented

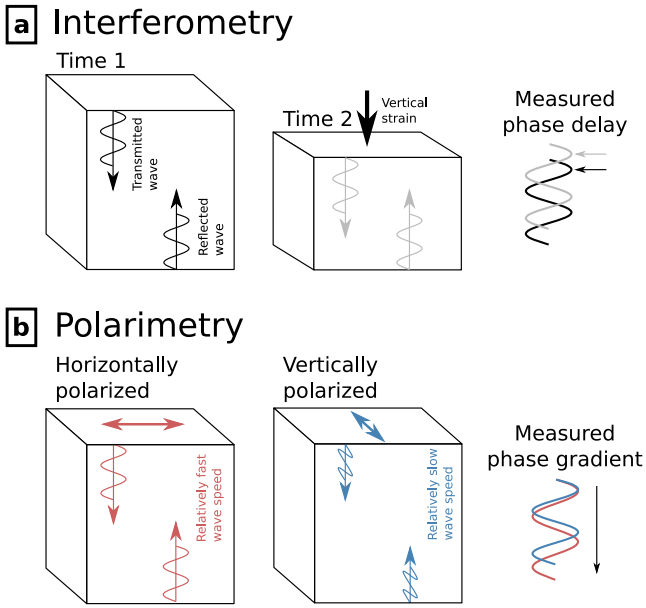

Figure 3. Illustration of the phase-based radar techniques used in this study. (a) Interferometry with a repeated acquisition in the same location but with some time separation, used to interpret vertical motion of reflecting interfaces relative to the instrument at the surface. (b) Polarimetry with a repeated acquisition at the same time but with different antenna orientation (polarization), used to interpret anisotropic crystal orientation fabric.

north-south. The acquisition locations, including precise antenna locations, were flagged for reoccupation and measured with precision GNSS as described above. We used a single attenuator at 20 dB and −4 dB gain for a 1-s ramped chirp from 200 to 400 MHz (range resolution 0.43 m). ApRES data were processed as described by Brennan et al. (2014) and implemented in ImpDAR (Lilien et al., 2020). For each acquisition, we stacked at least 1,000 raw chirps and performed a range conversion using the known transmit signal. Following Kingslake et al. (2014), we calculate phase uncertainty using a median noise phasor associated with the noise floor for returns from below the bed reflector.

2.3.1. Inference of the Ice Vertical Velocity From Radar Interferometry

We repeat ApRES acquisitions for measurements of englacial vertical velocity (Figure 3a) at 26 sites. We compare the repeated acquisitions using a zero-lag cross-correlation, C, calculated in a moving range bin of 100 samples. The coherence between acquisitions over the given window is the real component of the resulting cross-correlation, and the phase delay between acquisitions is the angle, $\phi = \arg(C)$. We unwrap this phase delay profile by adding or subtracting an integer multiple of 2π at each wrap discontinuity. Then, the observed layer motion (in m yr^{-1}) is the phase difference between acquisitions after converting to distance using the center frequency of the transmitted signal ($f_c = 300$ MHz). Because it is a relative velocity, we align it with the surface accumulation rate in meters ice equivalent per year (i.e., excluding firn compaction) for consistency in figure axes. The accumulation rate is inferred from depth variations in near-surface radar stratigraphy (see Fudge et al., 2022). Finally, we isolate the range and power of the bed reflection as the deepest (furthest range) peak in measured power for both acquisitions and confirm that this reflection has high coherence between acquisitions.

To compare between sites, we deconstruct each measured velocity profile in two ways. First, we calculate an upper-column vertical strain rate by linear regression of

$$\dot{\epsilon}_{zz} = \frac{1}{\Delta t}\frac{\partial \phi}{\partial z}\frac{c}{4\pi f_c \sqrt{\varepsilon}} \tag{1}$$

where Δt is the time between acquisitions, c is the vacuum wave speed, and ε is the permittivity of ice (3.15). We isolate this regression to the upper portion of the ice column ($z \leq 0.6H$) as has been done in prior studies (Kingslake et al., 2014). Second, we optimize the measured velocity profile to a Lliboutry (1979) shape factor,

$$w = \dot{a}\left(1 - \frac{p+2}{p+1}\zeta + \frac{1}{p+1}\zeta^{p+2}\right) \tag{2}$$

where ζ is the normalized depth below surface, $\frac{z}{H}$, H the full thickness of the ice column, $\dot{a}$ the accumulation rate at the surface, and p the shape factor that we use for optimization. For both the strain rate calculation and the shape factor optimization, we discard the shallow range bins less than 200 m depth due to the complexity of the firn compaction signal as well as the deep range bins with low coherence (<0.8).

2.3.2. Inference of the Crystal Orientation Fabric From Radar Polarimetry

Ice crystals have anisotropic permittivity (Matsuoka et al., 1997). The permittivity is ∼1% larger (slower wave speed) when the wave is polarized parallel to the crystal c axis and smaller (faster wave speed) when polarized along the basal plane. Therefore, subsurface returns from perpendicularly polarized waves may exhibit some phase delay due to the difference in wave speed through the ice (Figure 3b). When the radar antennas are polarized relative to the expected COF, measurable phase delays reveal information about COF strength and orientation.

21699011, 2025, 3, Downloaded from https://agupubs.onlinelibrary.wiley.com/doi/10.1029/2023JF007588 by Benjamin Hills - University Of Washington Lib , Wiley Online Library on [26/02/2025]. See the Terms and Conditions (https://onlinelibrary.wiley.com/terms-and-conditions) on Wiley Online Library for rules of use; OA articles are governed by the applicable Creative Commons License

21699011, 2025, 3, Downloaded from https://agupubs.onlinelibrary.wiley.com/doi/10.1029/2023JF007588 by Benjamin Hills - University Of Washington Lib , Wiley Online Library on [26/02/2025]. See the Terms and Conditions (https://onlinelibrary.wiley.com/terms-and-conditions) on Wiley Online Library for rules of use; OA articles are governed by the applicable Creative Commons License

The effectiveness of such polarimetric radar experiments on glacier ice has been demonstrated in theory (Fujita et al., 2006) and applied across Antarctica and Greenland to understand fabric development and ice-flow history (e.g., Brisbourne et al., 2019; Jordan et al., 2019, 2022; Young et al., 2021). Similar interpretations have been made based on seismic anisotropy in ice (Smith et al., 2017) and with a much longer history in the solid Earth (Savage, 1999). Since it is logistically easiest to polarize the wave in the *x*/*y* directions, with the wave propagating downward in the *z* direction, the most directly measurable fabrics are those with some *x*/*y* anisotropy. For example, a vertical girdle is measurable with *x*/*y* polarimetry, but a vertical pole is not (Rathmann et al., 2022). Model inversions which include both phase delay and reflectivity information may enable the identification of vertically oriented COFs (Ershadi et al., 2022), but here we focus only on the phase delay.

Alignment of the ApRES antenna polarization with the COF principal axes leads to two critical phenomena, both of which are encoded in the received signal. First, the cross-polarized acquisition measures minimal returned power (cross-polarized extinction; XPE) (Ershadi et al., 2022) because the wave does not depolarize as it moves through the ice column. The horizontally polarized wave will remain horizontally polarized and exhibit minimal power in the vertically polarized receive antenna. Second, there is a phase delay between perpendicularly polarized waves. A wave polarized parallel to the COF maximum (i.e., in line with most crystal *c* axes) travels slower than one perpendicularly polarized. The parallel wave therefore arrives at the receive antenna slightly later than the perpendicular wave, creating a phase delay, which increases with propagation depth into the ice. The depth gradient of that phase delay is related to the magnitude of *x*/*y* anisotropy. Note that we use the polarization notation from the literature where "*H*" indicates horizontally polarized (in line with the antenna array) and "*V*" indicates vertically polarized (perpendicular to the antenna array). Then, the co-polarized acquisitions are *HH* or *VV*, and the cross-polarized are *HV* or *VH* (see Figure 1 in Young et al., 2021).

The shallowest anisotropic fabric detectable in the ice column can be easily inferred based on extinction (Ershadi et al., 2022) or similarly with azimuthal symmetry in the phase gradients (Jordan et al., 2022). When the orientation remains consistent, and especially if it is well-aligned with the antenna array, it is feasible to extract depth-variable girdle strength through the full ice column (Zeising et al., 2023). However, with any change in the COF orientation it becomes more difficult to constrain using only extinction or depth-phase gradients because the wave has changed to an elliptical polarization by the time it encounters deeper layers of anisotropic ice. Forward modeling of the effects of a complex fabric could generate expected interferometric observations, but the results are non-unique since there can be anisotropy at the reflecting interface as well. Because of this complexity, we assume only a single anisotropic fabric orientation (along the XPE) and interpret our data accordingly.

We acquired *x*/*y* polarimetric ApRES data at 27 sites. As for the interferometry measurements, the transmit and receive antennas were separated by 10 m, with the array oriented north-south. Precise positions for both transmit and receive antennas were measured with GNSS, so the azimuthal orientation of the antenna array is accounted for. At each site, we stacked between 500 and 1,000 chirps in both co-polarizations as well as at least one cross-polarization and sometimes both (the cross-polarized terms are theoretically identical, so only one needs to be measured).

We use all four acquisitions in a rotational transform to define azimuthal radar images for each. Each measurement acquisition is an array of range bins, so rotating through all azimuths gives a total of four 2-dimensional images, one for each polarization. We estimate the orientation of *x*/*y* COF anisotropy (girdle orientation) by searching for the XPE axis at each range bin in the cross-polarized image. Knowing that the cross-polarized image is symmetric at $\pi/2$, we choose the XPE associated with a negative phase-depth gradient so that the *H* polarization is maximally aligned with the COF girdle axis. In the same manner as above, we calculate phase delay using the coherence between the co-polarized images (C_{HHVV}) (Jordan et al., 2019, Equation 13), now averaged over a moving 2-day window (we use a 200-m window in the range dimension but limit the azimuth window to a single trace so that the depth-phase gradient is not smeared across azimuths). The phase delay between co-polarized images is then $\phi_{\mathrm{HHVV}} = \arg(C_{\mathrm{HHVV}})$.

The desired variable, the phase-depth gradient, is most interpretable when the polarization axis is aligned with the girdle, so we extract the calculated phase delay along the XPE, $\phi_{\mathrm{xpe}}(z)$. The phase gradient at XPE is then directly proportional to the girdle strength (Jordan et al., 2019),

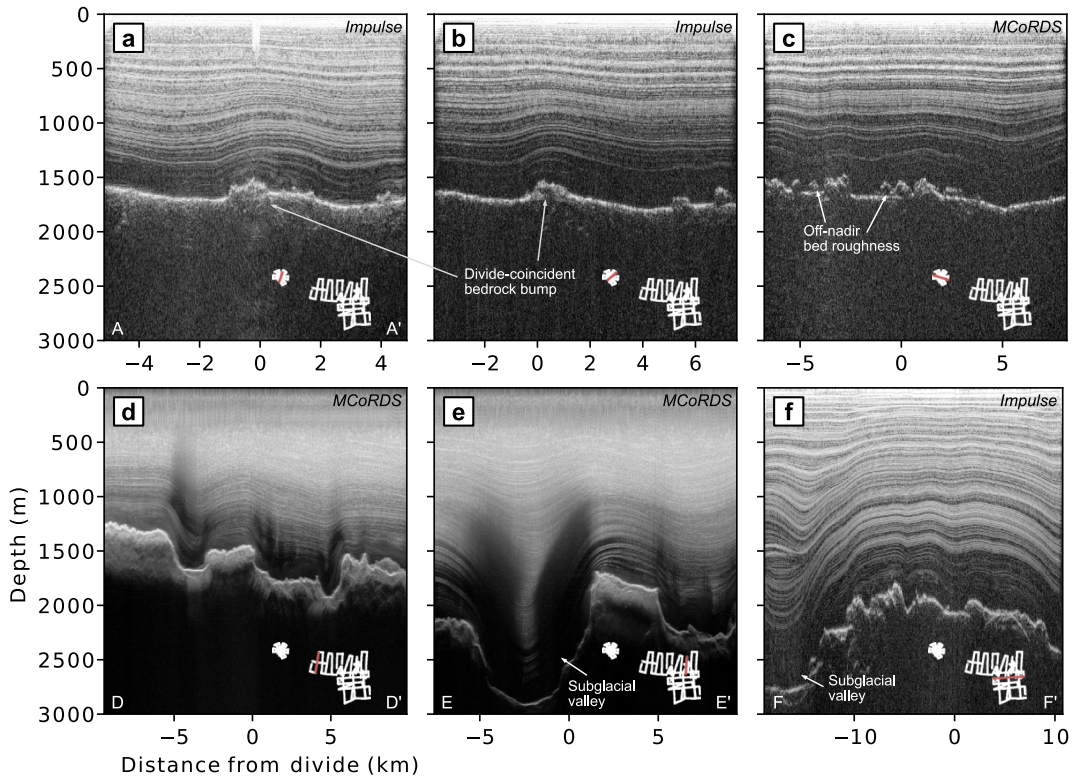

Figure 4. Radar profiles from HD Summit (a–c), Belt (d), East Dome (e), and South Ridge (f). Inset maps in the bottom right of each panel show all the ground-based radar profiles from this study (white) and the selected profile for that panel (red). For reference, see the corresponding radar profile locations in Figure 5b.

$$\lambda_2 - \lambda_1 = \frac{\partial \phi_{\mathrm{xpe}}}{\partial z} \frac{2c\sqrt{\varepsilon}}{4\pi f_c \Delta\varepsilon} \tag{3}$$

where $\Delta\varepsilon = 0.034$ is the difference in single-crystal permittivity between waves polarized parallel and perpendicular to the c axis, and λ_2 and λ_1 are the eigenvalues of the horizontal principal directions (with the remaining principal direction being assumed vertical and not considered here) of the crystal orientation tensor (as in Gerber et al., 2023). Since the measured phase delay is noisy, we unwrap the signal and apply a Savitsky-Golay filter to smooth the profile. We then calculate the phase gradient in depth by linear regression on a 200-m moving window. We limit this analysis to the depth of the observed phase nodes between 500 m (above which the firn should be expected to be isotropic) and 1,200 m (below which the uncertainty increases due to attenuation and loss of coherence between acquisitions). While confining the analysis to a depth span in this way restricts our ability to assess girdle changes with depth, extracting a single value per acquisition eases the regional comparison between sites which is our primary goal. Also, it gives us confidence since the XPE is relatively steady where the phase nodes are observed, whereas in cases with rapid COF rotations the interpreted XPE can diverge from the girdle axis (Jordan et al., 2022).

3. Geophysical Survey Results

3.1. Ice Geometry

The overall surface relief in the surveyed area spans from 2,530 to 2,620 m. The highest point is at HD Summit, with the secondary rise at East Dome ~15 m lower. Measured ice thicknesses range from 1,400 to 2,900 m (Figure 4). The thinnest and most uniform ice is at HD Summit (mean 1,665 m and total variation 390 m over the ~200 km^2 radial survey). The raised bed topography in the region surrounding HD Summit and extending toward the Belt is part of the Thiel Mountain Block (Winter et al., 2018). The thickest ice is in a large east–west subglacial

21699011, 2025, 3, Downloaded from https://agupubs.onlinelibrary.wiley.com/doi/10.1029/2023JF007588 by Benjamin Hills - University Of Washington Lib , Wiley Online Library on [26/02/2025]. See the Terms and Conditions (https://onlinelibrary.wiley.com/terms-and-conditions) on Wiley Online Library for rules of use; OA articles are governed by the applicable Creative Commons License

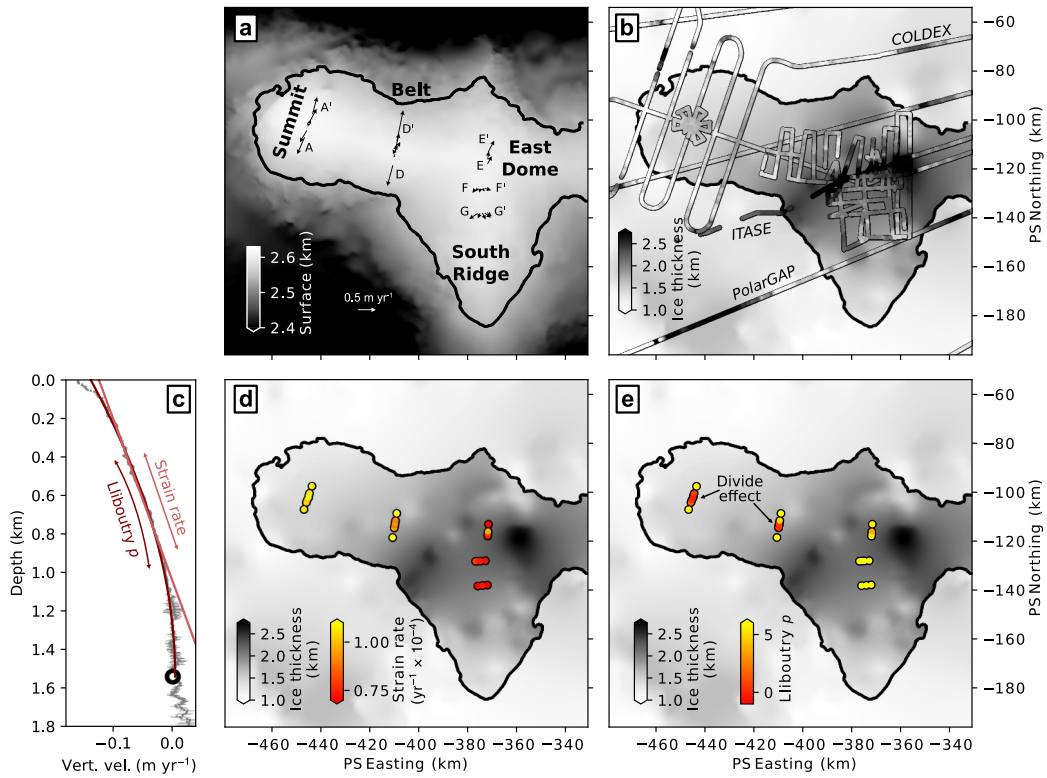

Figure 5. Regional overview of velocity and ice-thickness measurements. (a) Surface velocity vectors and surface elevation, with the thick outline as a single elevation contour. (b) Ice thicknesses from all profiling radar data are shown, with labels for those not specific to our ground survey. (c) An example vertical velocity profile with two parameterizations, linear for strain rate (Equation 1) and the Lliboutry (1979) shape factor (Equation 2). (d) Vertical strain rates calculated at each radar interferometry site. (e) Lliboutry (1979) shape factor calculated at each radar interferometry site. Low values of p indicate a divide effect. The base map in (b), (d), and (e) is ice thickness from BedMachine (Morlighem et al., 2020). For higher-resolution bed topography see Hoffman, Holschuh, et al. (2023).

valley at East Dome (Hoffman, Holschuh, et al., 2023). South Ridge is on the other side of that subglacial valley, on the Wisconsin Mountain Block. Both South Ridge and Belt have intermediate ice thickness, with the bed lifted out of the deep subglacial valley of East Dome but more bed relief than HD Summit.

3.2. Ice Flow

The measured ice flow, both surface velocities and englacial vertical velocities, are summarized regionally in Figure 5. Details specific to each region are described below. We give more attention to the measurements at HD Summit (A–A′) and Belt (D–D′) (Figure 6) since those have the highest data density and are the point of focus in subsequent sections (for measurements at East Dome and South Ridge see the Supporting Information S1).

Surface velocities are aligned with the surface gradient, as expected. At HD Summit (A–A′), seven surface velocities were measured along one transect, oriented perpendicular to the regional divide. Along that transect, ice flow is north-south spreading. Measured speeds are from 0 m yr^{-1} at the divide to 0.5 m yr^{-1} at the transect ends, 5 km to the north and south. The ice is spreading along this transect at 1.1×10^{-4} yr^{-1}. The eight surface-velocity measurements at Belt (D–D′) have similar behavior to HD Summit, only with closer spacing near the divide. The surface strain rate is slightly higher, 1.5×10^{-4} yr^{-1}. At South Ridge (F–F′ and G–G′), all flow vectors have some southward velocity component, but the predominant flow pattern is east–west spreading with a surface strain rate of 6.1×10^{-5} yr^{-1} (F–F′) and 9.3×10^{-5} (G–G′). At East Dome (E–E′), the surface velocity vectors are not well aligned with the transect. Instead, a component of ice flow is toward the east, aligned with the bedrock valley.

21699011, 2025, 3, Downloaded from https://agupubs.onlinelibrary.wiley.com/doi/10.1029/2023JF007588 by Benjamin Hills - University Of Washington Lib , Wiley Online Library on [26/02/2025]. See the Terms and Conditions (https://onlinelibrary.wiley.com/terms-and-conditions) on Wiley Online Library for rules of use; OA articles are governed by the applicable Creative Commons License

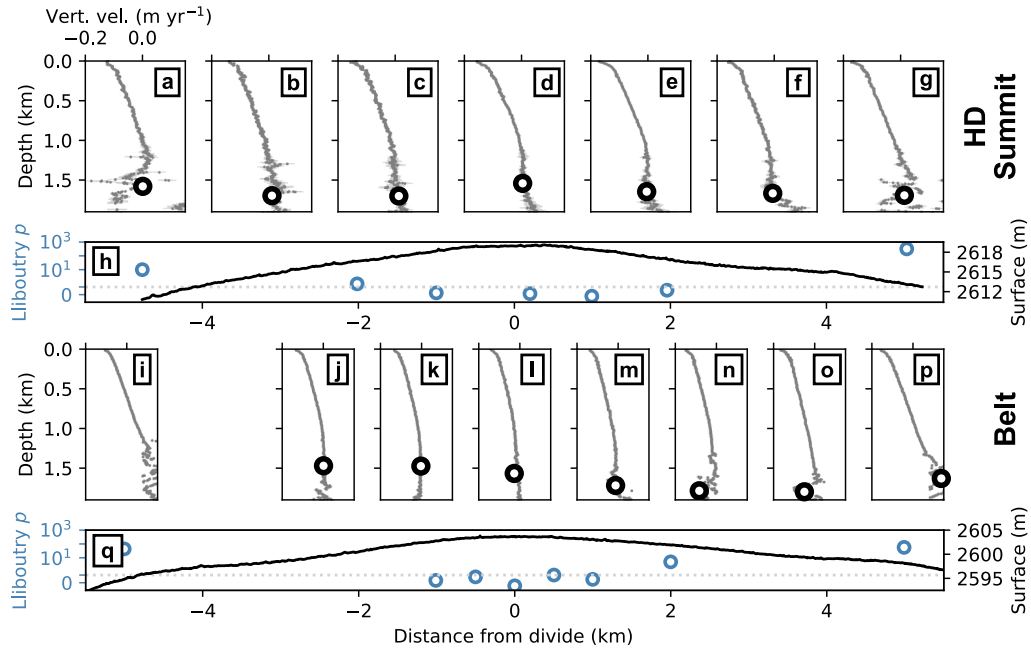

Figure 6. Hercules Dome Summit and Belt present-day ice flow and geometry measurements along profiles A–A′ and D–D′ in Figure 5, respectively. (a–g) Vertical velocity profiles at 7 sites across HD Summit. Gray dots represent a calculated velocity within a single range bin and the associated horizontal line the uncertainty within that bin. The larger black dot is the vertical velocity of the interpreted bed reflector. Note that the phase offset measurement gives a relative velocity, which has been referenced to the surface accumulation rate as described in the text. (h left axis) Vertical velocity optimization to the Lliboutry (1979) p value (Equation 2) for each profile (a–g). (h right axis) Surface elevation profile measured with kinematic Global Navigation Satellite System profiling. (i–p) As in (a–g) but for vertical velocity profiles at Belt. (q) As in (h) but for the transect at Belt.

Englacial vertical velocity profiles are also mostly consistent across the dome. Each has its greatest downward speed at the ice surface, where new snow is deposited. The depth gradient, or vertical strain rate, is also greatest within the upper ice column ($z < 200$) which is subject to firn compaction. In the middle of the ice column ($200 < z < 0.6H$) the vertical velocity profiles are quasi-linear (approximately uniform thinning). In this portion of the ice column with uniform thinning, the magnitude of the strain rate is most strongly dependent on the ice thickness. That is, thin ice necessitates a higher strain rate for the same accumulation and outward spreading. In the lower ice column ($z > 0.6H$), the measured velocity behavior is less consistent between sites, even qualitatively. Some sites approach zero velocity nonlinearly (small p), as would be expected in a region of divide flow (Fudge et al., 2022; Kingslake et al., 2014). Other sites show increasing strain rate toward the bed which is not expected but will be described and interpreted in Section 5.1. Deep reflections from sites in the thickest regions of Hercules Dome also lose coherence, making it challenging to observe vertical velocity below $\sim 1200 - 1500$ meters.

At HD Summit there are seven vertical velocity profiles along A–A′, with the four from the divide to the north originally published in a prior study (Fudge et al., 2022). The additional 3 sites to the south do not qualitatively change the interpretation presented there. That is, the vertical velocity profiles are most linear ("flank-like" flow) away from the divide and most nonlinear ("divide-like" flow) toward the divide, especially slightly north of the divide. This distinction is shown quantitatively in the optimized p values where the most nonlinear vertical velocity profiles (smallest p) are at and just north of the divide.

Belt has similar vertical velocities to HD Summit. Here, 8 profiles were acquired along D–D′, with closer site spacing (500 m) near the divide than in A–A′. The divide-flow effect present in the HD Summit transect is also present here. All vertical velocity profiles within 1 km of the divide are similar, and all are nonlinear. Any trend among those near-divide sites is more likely associated with bed features than a variation in the divide-flow effect. Away from the divide, the profile two km to the north (Figure 6o) is trending toward linear, and those furthest from the divide (Figures 6i and 6p) have reversed curvature, showing signs of significant compression near the ice

21699011, 2025, 3, Downloaded from https://agupubs.onlinelibrary.wiley.com/doi/10.1029/2023JF007588 by Benjamin Hills - University Of Washington Lib , Wiley Online Library on [26/02/2025]. See the Terms and Conditions (https://onlinelibrary.wiley.com/terms-and-conditions) on Wiley Online Library for rules of use; OA articles are governed by the applicable Creative Commons License

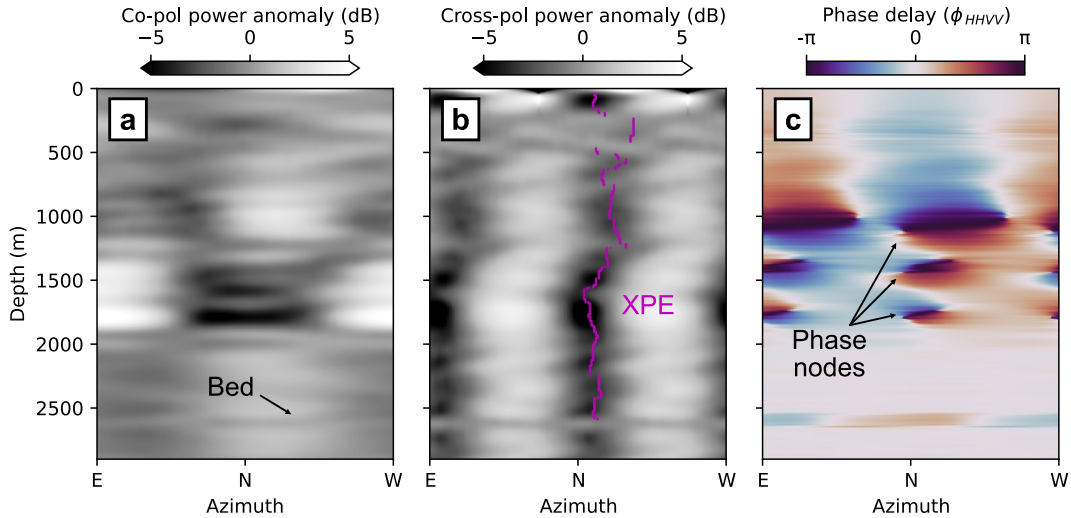

Figure 7. An example polarimetry acquisition from East Dome (see site label in Figure 8) with the co-polarized power (a), cross-polarized power (b), and co-polarized phase delay (c). Power images are shown as an anomaly from the mean for each range bin. The magenta dots in panel (b) are the inferred XPE axis orientation for each range bin.

base. Again, this result is not physical (vertical strain rate should not increase near the bed) and we discuss the reason for the measurement below.

Vertical velocity profiles at South Ridge are more consistent with one another, all being approximately linear (Figures S5 & S6 in Supporting Information S1). The ice column is also thicker here, so deep reflections are lost due to low coherence between ApRES acquisitions. If there is a nonlinear effect of divide-like flow, it is not observable and we do not expect it to be due to this loss of coherence. At East Dome, vertical velocities are again approximately linear and coherence is lost in the deepest layers of the thick ice column (Figure S7 in Supporting Information S1). Here, no divide-flow effect is observed, nor was it expected since the surface divide is weak. The greatest vertical strain rate within profiles at East Dome is at the site 2 km to the north of the surface divide, which is directly over the edge of the large bedrock valley.

3.3. Crystal Orientation Fabric

The general characteristics of each polarimetry acquisition are consistent between sites (Figure 7). The co-polarized phase delay is approximately 0 for near-surface reflections which is expected since it depends on the propagation distance through the ice. Phase gradients are also weak in the uppermost ∼500 m which is again expected since snow is deposited randomly (the bulk snow therefore being isotropic) and near-surface ice has not been sufficiently strained to develop significant anisotropy. At least one ϕ_{HHVV} node (corresponding to a phase delay of 1 period) is observed in every acquisition, although the depth, orientation, and magnitude are different for each. For most acquisitions, the depth of the first ϕ_{HHVV} node is ∼700–1,200 m.

As described in Section 2.3.2, we can use the azimuth of cross-polarized extinction (XPE) to infer girdle orientations at each site. We find that there are two distinct girdles in the region, rotated ∼90° from one another (Figure 8). Sites to the west (HD Summit and Belt) have west-northwest XPE, aligned with the primary ice divide. Sites at South Ridge have north-northeast XPE, aligned with that secondary divide. The site at East Dome has north-northwest XPE, aligned with the axis of the valley in the bed geometry. This rotation of the girdle orientation about the triple divide was expected based on the regional ice flow.

For HD Summit and Belt, where most of the polarimetry experiments were conducted, the interpreted girdle orientations indicate fabric development and alignment consistent with north-south spreading perpendicular to the divide (Figures 8b and 8c). Differences between acquisitions within these regions are subtle and require a quantitative comparison (Figure 9). From HD Summit along A–A′, the strongest calculated girdle strengths are at the divide and 1 km north of the divide, and the weakest girdles are at the sites furthest from the divide. An

21699011, 2025, 3, Downloaded from https://agupubs.onlinelibrary.wiley.com/doi/10.1029/2023JF007588 by Benjamin Hills - University Of Washington Lib , Wiley Online Library on [26/02/2025]. See the Terms and Conditions (https://onlinelibrary.wiley.com/terms-and-conditions) on Wiley Online Library for rules of use; OA articles are governed by the applicable Creative Commons License

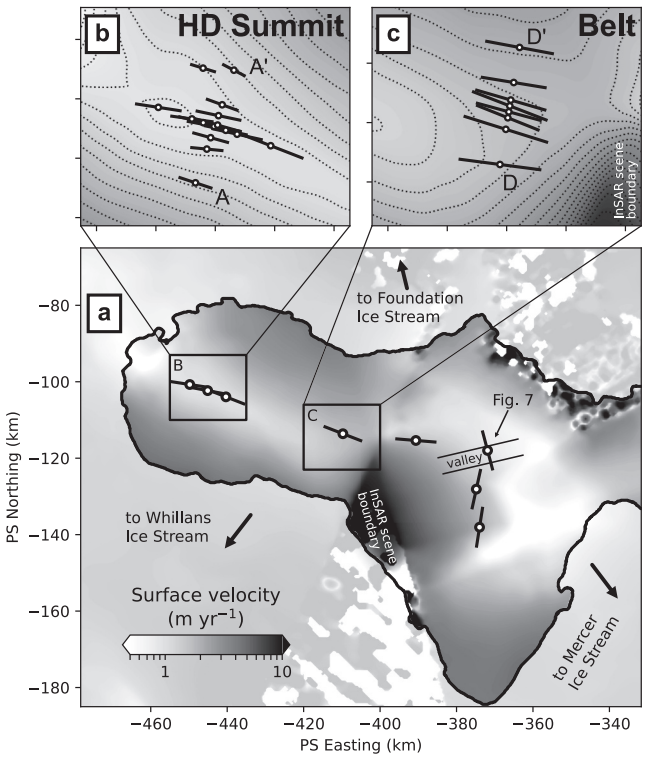

Figure 8. A map view of radar polarimetry results. Dots show polarimetry acquisition locations with lines indicating the inferred girdle axis (line orientation) and representative girdle strength (line length). The regional map (a) shows only acquisitions from select sites around the dome, while the inset maps show all acquisitions from HD Summit (b) and Belt (c). The base map is ice-surface velocity (Mouginot et al., 2019). The surface velocities are shown here as a reference but should be interpreted cautiously because they are known to be problematic at these slow flow speeds as can be seen by the labeled InSAR scene boundary.

additional seven sites with polarimetric acquisitions form a transect *along* the divide at HD Summit (Figure S8 in Supporting Information S1). These sites have more consistent phase gradients than the across-divide transect, with one prominent outlier to the east (toward Belt). That location has a slight negative phase gradient in the near surface and a deeper ϕ_{HHVV} node with positive phase gradient. Along D–D′ at Belt there is a slight increase in girdle strength at the divide, but even greater strength to the south. Additionally, the typical girdle strength here is approximately double that at HD Summit (see the change in *y*-axis between Figures 9h and 9q).

4. Analysis: Characteristic Timescales of Crystal Fabric Evolution

In this section, we contextualize the geophysical results with a mathematical model of COF evolution. Following Rathmann et al. (2021) (as implemented in *specfab*), the model is a continuum representation of crystal *c*-axis distribution in spherical coordinates. The time rate of change of the *c*-axis distribution depends on the stress/strain regime (Lilien et al., 2023; Placidi et al., 2010; Rathmann & Lilien, 2021; Richards et al., 2021),

$$\frac{D\psi}{Dt} = -\nabla_{S^2} \cdot \left(\psi \dot{\boldsymbol{c}}\right) + \Omega \nabla^2_{S^2} \psi + \Gamma \psi \tag{4}$$

where $\boldsymbol{c}$ is the *c*-axis orientation of an arbitrary ice crystal, $\dot{\boldsymbol{c}}$ is the time rate of change of that crystal orientation, and ψ is the distribution of *c*-axes in spherical coordinates. The term on the left-hand side is a material derivative, with COF being advected through the macroscopic domain, and the three terms on the right-hand side represent lattice rotation, $-\nabla_{S^2} \cdot (\psi \dot{\boldsymbol{c}})$, rotation recrystallization, $\Omega \nabla^2_{S^2} \psi$, and dynamic recrystallization, $\Gamma \psi$. We base our parameter choices on model optimizations to laboratory experiments, $\Omega = 0.15$ (Richards et al., 2021), and for dynamic recrystallization in cold ice, $\Gamma_0 = 0.1$ (see the parameter sensitivity test in Supporting Information S1 for more detail). This model enables us to relate measured present-day strain rates (both vertical and surface strain) to COF results from radar polarimetry which correspond to a strain history.

We give particular emphasis to modeled timescales to determine how quickly the measured vertical girdle at HD Summit could have been established under the present-day strain regime, and how long it would take to overprint the COF from a historical strain regime. In other words, we want to know how long an ice dynamic change might be preserved in the COF; and conversely, how long the dynamically consistent COF that we observe indicates stability at Hercules Dome. Lab results show that COF is sufficiently developed to cause a transition to tertiary creep by a cumulative strain of approximately 0.1 (Budd & Jacka, 1989), so in situ COF (from direct ice samples) should be measurable at that stage. With additional strain, the COF will continue to evolve and, in the case of a steady strain regime, eventually converge onto some equilibrium state, with the timing depending on the initial state, the strain rate, and the strain geometry. We define the equilibration time as that at which the COF has developed to within $\frac{1}{e}$ of its equilibrium state, although the COF does continue to change somewhat afterward. Note that our convention is for an "engineering strain," $\frac{\Delta L}{L_0}$, and is distinct from the true cumulative strain, $\int_0^t \frac{\delta L}{L}$, which is logarithmic.

For each model scenario we (i) spin up the COF state from isotropic into some hypothetical past strain regime, and (ii) change the prescribed strain regime to that of the present day and run the model forward until it reequilibrates (Figure 10). To keep the model experiment simple, we consider the "present-day" setting confined compression, and select from one of three regimes for past strain: (i) confined compression but rotated from present day; (ii) less confined than present day (with the limit of completely unconfined having an along-divide flow component equal to the cross-divide component, 0.5, a perfectly round dome); or (iii) migrated from present day (which we treat as

21699011, 2025, 3, Downloaded from https://agupubs.onlinelibrary.wiley.com/doi/10.1029/2023JF007588 by Benjamin Hills - University Of Washington Lib , Wiley Online Library on [26/02/2025]. See the Terms and Conditions (https://onlinelibrary.wiley.com/terms-and-conditions) on Wiley Online Library for rules of use; OA articles are governed by the applicable Creative Commons License

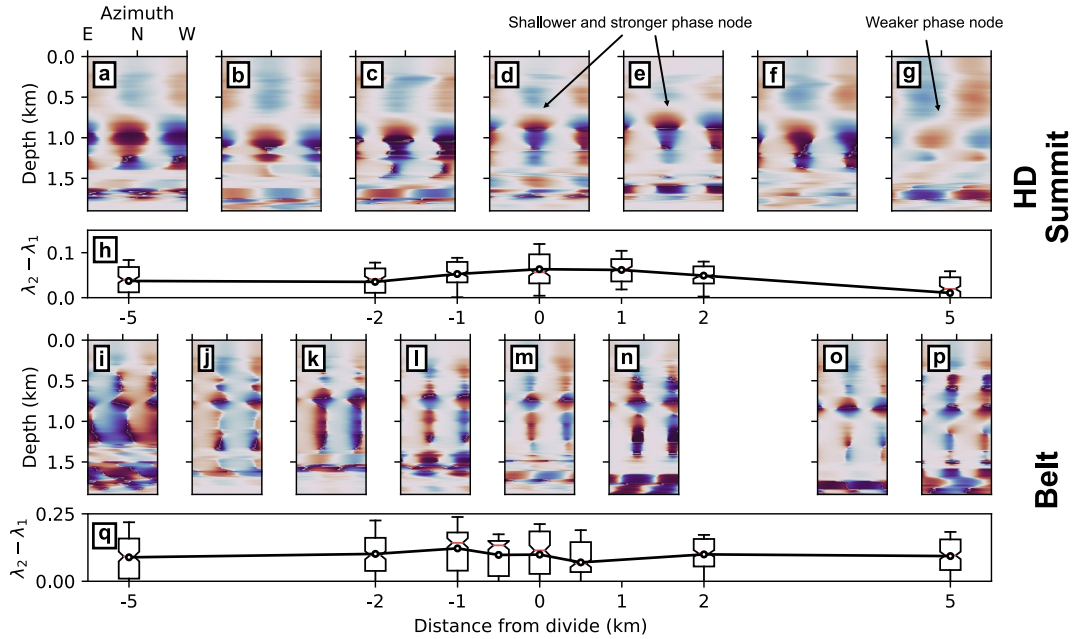

Figure 9. HD Summit (a–h) and Belt (i–q) radar polarimetry measurements along profiles A–A′ and D–D′ in Figure 8, respectively. (a–g & i–p) Co-polarized phase images are as in Figure 7c. (h and q) Box plot for extracted girdle strength along each XPE profile, calculated from the phase gradient (Equation 3).

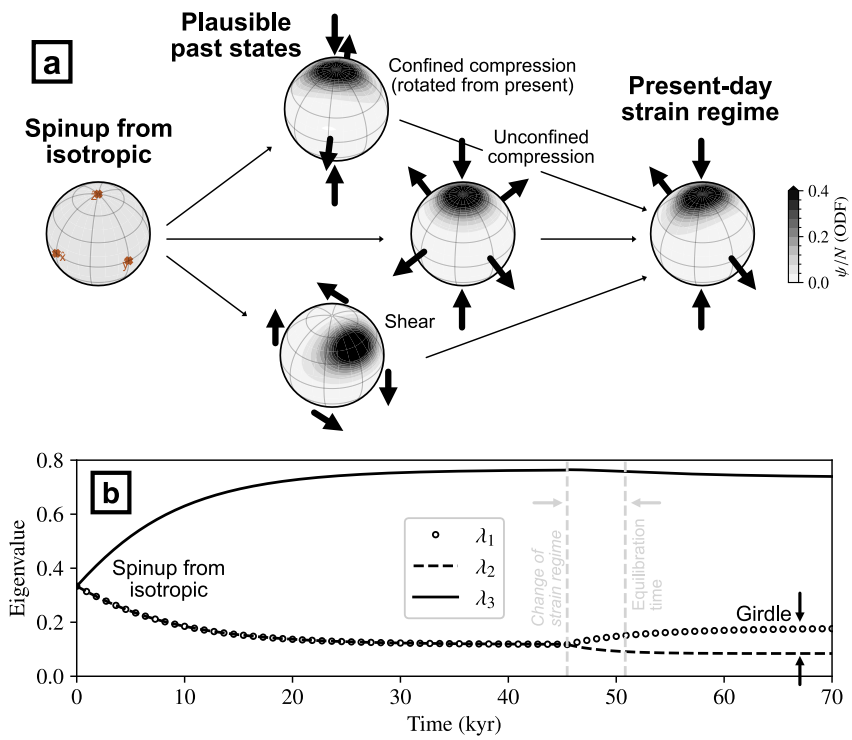

Figure 10. Visualization of the model analysis. (a) A series of orientation distribution functions with the grayscale representing the number of crystal *c* axes as a fraction of the whole (see Rathmann et al. (2021)). As explained in the text, the progression is from (i) isotropic to (ii) some plausible past state to (iii) the present-day strain regime. Large black arrows show the dominant direction of ice flow in each strain regime. (b) Eigenvalues through time for spin-up in unconfined compression and then a change to the present-day confined compression.

21699011, 2025, 3, Downloaded from https://agupubs.onlinelibrary.wiley.com/doi/10.1029/2023JF007588 by Benjamin Hills - University Of Washington Lib , Wiley Online Library on [26/02/2025]. See the Terms and Conditions (https://onlinelibrary.wiley.com/terms-and-conditions) on Wiley Online Library for rules of use; OA articles are governed by the applicable Creative Commons License

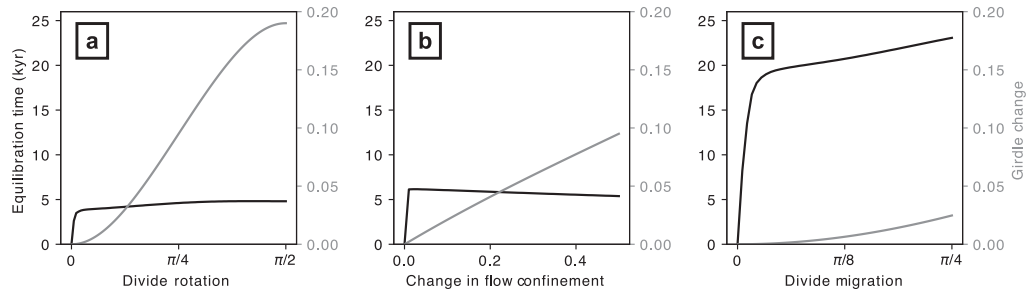

Figure 11. Crystal orientation fabric evolution for a change in strain regime from three spin-up scenarios. (a) Divide rotation where 0 is at the same orientation as present day, and $\pi/2$ is a perpendicular divide in the past. (b) Changing the confinement of flow along the divide, where 0 is no along-divide flow and 0.5 is 50% or fully unconfined (a round dome). (c) Divide migration which introduces a component of shear, 0 being no shear and $\pi/4$ all shear. Equilibration time from the spin-up state to the updated strain regime is shown in black. The magnitude of change in the x–y girdle (i.e., $\lambda_2 - \lambda_1$ at present minus $\lambda_2 - \lambda_1$ in the past strain regime) is shown in gray.

an addition of some component of vertical shear, $\pi/4$ being all shear). In Figure 11, we give the results from forward simulations for a range of plausible dynamic changes in all three regimes. Since we identify the equilibration time based on a relative adjustment toward equilibrium COF, times are relatively consistent for each type of change (except when there is no change so stabilization would take no time). Divide rotation results in the strongest girdle change, unsurprisingly since the girdle axes are flipped at a rotation of $\pi/2$. The equilibration time for a rotation is ~5 thousand years. Changes in the along-divide flow component (divide-like vs. dome-like) are similar to rotations although with approximately half the magnitude of girdle change. Divide migrations (adding a component of vertical shear) are the weakest girdle change (since vertical shear also produces a girdle, only tilted) but takes the longest to equilibrate, ~20 thousand years. The lower end for time to equilibration among these three hypothetical historical strain scenarios is approximately five thousand years or mid Holocene. Since equilibration times are proportional to the strain rate, the results given here could be generalized to other areas by multlying the strain rate (with a nondimensional equilibration time, $\tau = t\dot{\epsilon}$, or ~0.5 based on our model result and measured strain rates).

5. Discussion

5.1. Geophysical Measurement Trends and Outliers

At HD Summit, Belt, and South Ridge, the present-day ice flow, as measured by repeat ApRES and surface GNSS measurements, and COF girdle orientation and strength, as measured by radar polarimetry, are all generally consistent with the expected ice-flow behavior given the ice-surface geometry. These dynamics also correspond to the regional bed geometry, with the surface triple divide situated over two bedrock highs separated by a deep glacial valley. The measured surface velocities point away from the surface divide (Figure 5a). Vertical velocity profiles trend from sublinear (small p) at the surface divide toward linear away from the divide (as expected for divide-to-flank flow). The COF indicates a divide-aligned girdle (i.e., east–west girdle for sites at HD Summit and Belt but north-south girdle for sites at South Ridge). COF is therefore aligned with the measured ice flow since a divide-aligned girdle would develop under conditions where vertical thinning and cross-divide spreading are the dominant flow patterns. The magnitude of the girdle varies slightly between sites, but the orientation is consistent with the divide orientation for every site. The observed girdle has greater magnitude at Belt as compared to HD Summit. This is also not surprising since Belt is confined to extension in a single direction (across the divide) whereas HD Summit has a dome-like shape so will have some amount of divide-parallel spreading (especially for sites further from the divide).

The only significant outlier to the consistency between ice flow and ice geometry for sites at HD Summit, Belt, and South Ridge are the two vertical velocity profiles in the ApRES transect at Belt, those furthest from the divide, at 5 km north and south (Figures 6i and 6p). Those two vertical velocity profiles have reversed curvature from those sites nearest the divide. We interpret these two sites as having a Lagrangian effect from dipping reflectors since they are both situated at the edge of a large bedrock bump, and they have a significantly faster surface velocity than sites nearer to the divide. As explained by Hills et al. (2022), vertical shear results in horizontal

21699011, 2025, 3, Downloaded from https://agupubs.onlinelibrary.wiley.com/doi/10.1029/2023JF007588 by Benjamin Hills - University Of Washington Lib , Wiley Online Library on [26/02/2025]. See the Terms and Conditions (https://onlinelibrary.wiley.com/terms-and-conditions) on Wiley Online Library for rules of use; OA articles are governed by the applicable Creative Commons License

21699011, 2025, 3, Downloaded from https://agupubs.onlinelibrary.wiley.com/doi/10.1029/2023JF007588 by Benjamin Hills - University Of Washington Lib , Wiley Online Library on [26/02/2025]. See the Terms and Conditions (https://onlinelibrary.wiley.com/terms-and-conditions) on Wiley Online Library for rules of use; OA articles are governed by the applicable Creative Commons License

motion over dipping reflectors which causes an apparent vertical velocity. That these two sites in particular exhibit this effect is unsurprising, since they have a faster surface velocity (more vertical shear) than others in the transect and each is on the stoss side of a bedrock bump.

The East Dome ice-surface velocity and englacial vertical velocity seem to be controlled by the geometry of the bedrock valley. Surface velocities point slightly off the surface gradient with a component along the valley, and the vertical strain rate is greatest at the valley edge. Only one polarimetry acquisition was taken at East Dome and that was directly over the valley. The resulting phase gradient at this site is more uniform with depth than at any other site, with three ϕ_{HHVV} nodes along the XPE axis (Figure 7c). The unmatched uniformity and deeper observed ϕ_{HHVV} nodes may be a result of this being the site with the thickest ice column. The girdle itself is aligned perpendicular to the valley axis which is consistent with longitudinal extension or vertical shear in that direction.

Our polarimetry acquisitions lose phase coherence deep in the ice column (below ∼1,500 m). Several factors likely contribute to this loss of signal. Warm temperatures for the deepest ice could lead to increased recrystallization and a less consistent COF, possibly in less predictable ways. Alternatively, significant phase delay could eventually cause decorrelation across range bins, but the co-registration method (Zeising et al., 2023) did not improve our result. Instead, we argue that those deep reflections are sufficiently attenuated to no longer be comparable, especially since the time-based ApRES interference seems to lose coherence at a similar depth.

To the northwest of HD Summit, beyond our ApRES and GNSS surveys, there are subtle indications of another subsurface valley that routes ice in a direction oblique to the regional surface gradient. This feature is most prominent in the airborne radar profile (Figure 5b), but upstream indications of channelization into a bedrock valley are seen in both the ground-based profiling radar and as a subtle expression in the surface topography. The direction of the valley would be consistent with routing flow toward the western tributary of Foundation Ice Stream even though there is no obvious indication of that in the present-day surface velocity measurements. The polarimetry measurements at HD Summit have no indication of a shift in the girdle axis toward this west valley. The presence of this valley may influence divide behavior during periods when the ice sheet was bigger or smaller, so we include it in our discussion of COF evolution timescales in Section 5.3.

5.2. West Antarctic Ice Sheet Dynamics From Glacial to Holocene Periods

The persistence of Hercules Dome as a steady divide between the Ross and Ronne ice shelves depends on (i) the ice flux into the system by precipitation, (ii) the ice flux out of the system, in this case mainly by melt and discharge in the Ross and Ronne ice shelves, and (iii) the ice flux from the divide region toward the ice shelves, controlled by the underlying bedrock topography and mechanics of glacier flow. When the ice sheet is in equilibrium these three fluxes balance and the position of features like the ice divide remain fixed. When one of these fluxes change, for instance during ice-sheet retreat in the Holocene, the other fluxes change in response and the position of features like divides and the grounding zone of marine outlet glaciers can change. In this section, we look at how climate changes associated with the transition out of the LGM into the Holocene affect the ice sheet's interior flux response. We consider whether there was mismatch in deglaciation timing between the two ice shelves and whether that could have had an upstream effect, potentially shifting or rotating the divide in a way that would be preserved in the present-day ice at Hercules Dome.

At the LGM, sea level was ∼100 m lower than today (Spratt & Lisiecki, 2016). Ice likely filled the Ross and Weddell seas, and paleo-ice-sheet models estimate that ice was grounded all the way to the continental shelf break (e.g., Golledge et al., 2012). As the global climate warmed into the Holocene, models and observations both show that the grounding line retreated toward today's position (Johnson et al., 2022), but the timing and detailed characteristics of this retreat for both the Ronne and Ross ice shelves are difficult to know precisely since they are controlled by many factors such as bed geometry near the grounding line (Huybers et al., 2017) and melt rates beneath the ice shelf (Whitehouse et al., 2017). We briefly describe the retreat scenarios given in the literature, formulated from both models and observations, before describing the simulated ice-sheet configurations we use to understand the ice-flow history at Hercules Dome and how the modeled dynamics compare to the strain histories we construct from radar polarimetry observations.

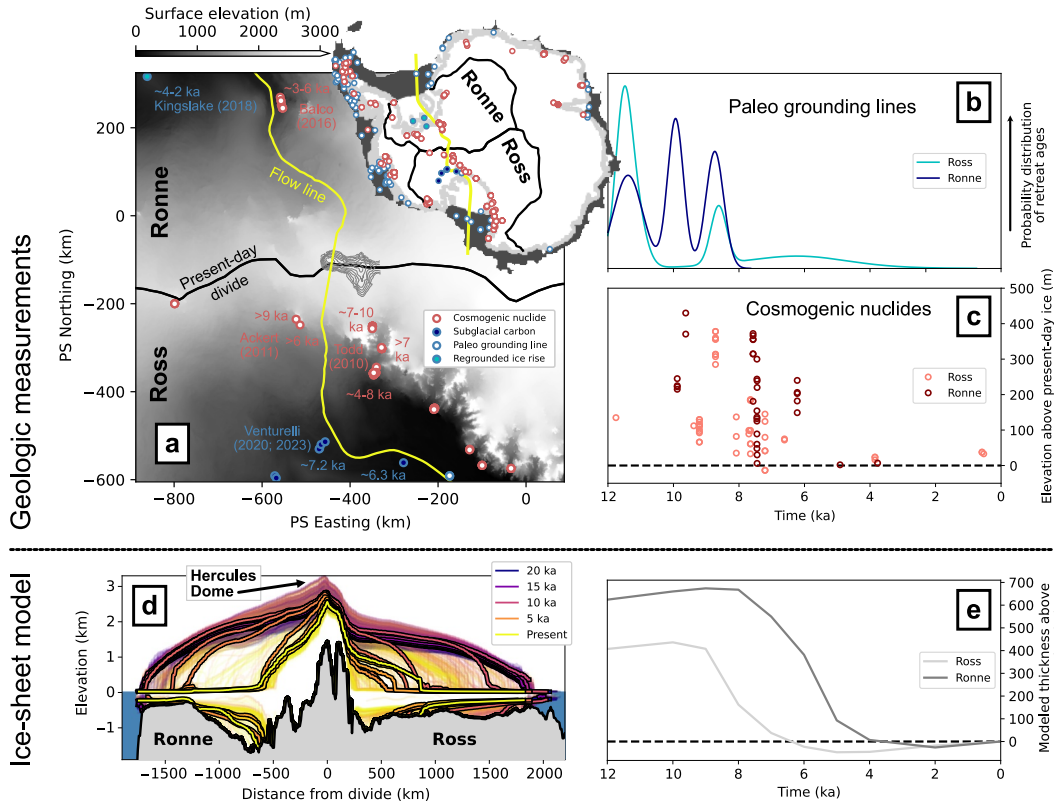

Figure 12. Evidence from prior studies for variable deglaciation timing between the Ross and Ronne basins. (a) Map of geologic measurement sites in the vicinity of Hercules Dome. At select points discussed in the text, annotations are provided for exposure ages (red) and regrounding timing (blue). Surface elevation and contours are as in Figure 2a. Inset continent-wide sites for exposure ages (Balco, 2020) and paleo grounding lines (Jones et al., 2022) with present-day ice extent (white), grounding line (light gray), continental shelf (dark gray), and the Ross/Ronne basins (black). (b) Deglaciation timing with a distribution of retreat ages from paleo grounding lines as in Jones et al. (2022). (c) Deglaciation timing from cosmogenic nuclide exposure ages for samples collected from a range of heights above the present day ice surface. (d) Modeled cross-sectional profiles (Albrecht et al., 2020b) along the flow line plotted in panel (a). All model ensemble members and all output time steps are shown, with the best-fit case outlined in black. Gray is bedrock and blue is ocean. (e) Mean basin-wide thickness above present day for the best-fit model ensemble member in (d).

Historical ice geometries and grounding-line locations can be constrained by a variety of measurements and proxies including exposure ages (Stone et al., 2003), sea-level change and isostatic rebound (Mitrovica et al., 2001), subglacial sediments and geomorphology (Kingslake et al., 2018), and englacial structures (Conway et al., 2002; Siegert et al., 2013). From these observations, we know that the Antarctic Ice Sheet was at least hundreds of meters thicker during LGM, both in the Weddell Sea (Ronne) (Nichols et al., 2019) and in the Ross (Anderson et al., 2014). Some studies show quasi-steady and monotonic grounding line retreat through the Holocene and to today's position (Conway et al., 1999), but more recent work suggests that the maximum extent of retreat was actually further inland than today ("over-retreat") (Johnson et al., 2022). The extent of over-retreat and subsequent readvance is thought to be larger on the Ross side Siple than the Ronne side (Kingslake et al., 2018). The flat bed of the Siple and Gould Coast ice streams makes them more sensitive to marginal forcing and glacial isostatic adjustment, and therefore their grounding line can be expected to move relatively large distances even with only subtle changes in the ice flow or climate forcing. Such rapid and transient changes in grounding-line position may not be expected to propagate all the way up to the divide position, while a persistent change perhaps could be.

Nearest to Hercules Dome, the best historical ice geometry constraints come from two sources, exposure ages and subglacial lake sediments (Figure 12a). Exposure age samples have been collected from three nearby outcrops. First, in the mountains adjacent to Reedy Glacier the peak ice thickness occurred between ~17–9 ka (depending on the specific outcrop), the onset of thinning occurred ~13 ka, and there were many exposures between ~7–10 ka

21699011, 2025, 3, Downloaded from https://agupubs.onlinelibrary.wiley.com/doi/10.1029/2023JF007588 by Benjamin Hills - University Of Washington Lib , Wiley Online Library on [26/02/2025]. See the Terms and Conditions (https://onlinelibrary.wiley.com/terms-and-conditions) on Wiley Online Library for rules of use; OA articles are governed by the applicable Creative Commons License

21699011, 2025, 3, Downloaded from https://agupubs.onlinelibrary.wiley.com/doi/10.1029/2023JF007588 by Benjamin Hills - University Of Washington Lib , Wiley Online Library on [26/02/2025]. See the Terms and Conditions (https://onlinelibrary.wiley.com/terms-and-conditions) on Wiley Online Library for rules of use; OA articles are governed by the applicable Creative Commons License

(Todd et al., 2010). Second, in the Pensacola Mountains to the north of Foundation Ice Stream the peak ice thickness is ∼17–9 ka (as for Reedy) but with slightly later onset of thinning at ∼11 ka and some more recent exposures at ∼3–6 ka (Balco et al., 2016). Third, the Ohio Range to the southwest of Hercules Dome has peak ice thickness at ∼10 ka and some younger exposures at ∼6–9 ka (Ackert et al., 2011).

Subglacial lake sediments were recovered from both Whillans Subglacial Lake (SLW) and Mercer Subglacial Lake (SLM), which occupy the two ice stream drainages that form the east–west divide at South Ridge, Hercules Dome. Critical to the story of stability at South Ridge, dated sediments from these subglacial lakes both indicate grounding line retreat past their present-day position followed by readvance. SLW was connected to the ocean cavity until ∼7.2 ka (Venturelli et al., 2020) and SLM ∼6.3 ka (Venturelli et al., 2023). The close off of these subglacial lakes came earlier than estimated readvance on the Ronne side, where ice-rise regrounding has been dated to the late Holocene, ∼2–4 ka (Kingslake et al., 2016, 2018).

Together, these geologic measurements show an offset in deglaciation timing by ∼2–4 thousand years between Ross and Ronne basins. Still, the full history is difficult to interpret since these point measurements can only be collected in select locations where either rock outcrops emerge through the ice or direct samples can be recovered from subglacial lakes. To develop a more distributed sense of deglaciation, we now discuss output from a two-part continental-scale modeling study which includes a 256-member ensemble for deglaciation into the Holocene (Albrecht et al., 2020a, 2020b). The model ensemble spans a range of physically plausible values for four unknown model parameters: ice viscosity (creep enhancement), basal-sliding plasticity (bed exponent), precipitation forcing, and mantle viscosity (for isostatic rebound). The "best-fit" ensemble member was chosen based on misfit to measurements of both present-day and paleo conditions. We note that the relatively coarse grid resolution in these model experiments does not adequately capture the relief that defines our measurements of the subglacial landscapes beneath Hercules Dome. We do not interpret any model result as the truth of a past ice-sheet state. Rather, we use the model output to understand the downstream forcing from ice-shelf melting and discharge (i.e., the ice flux *out* of the system as mentioned above). Specifically, we investigate the range in deglaciation scenarios for the Ross and Ronne ice shelves and use those to discuss drawdown forcing and associated divide stability at Hercules Dome.

Every member of the model ensemble starts from a fully glaciated state at LGM, where the ice sheet is grounded to the continental shelf edge. The timing of deglaciation from LGM to today depends on the parameter choice for a given ensemble member (Figure 12d). Of the 256 model ensemble members 137 members show the Ross Ice Shelf retreating before the Ronne and only 14 show the Ronne retreating first (with the remaining 104 showing initial retreat at the same time step). Note that output was only every 5 thousand years for these ensemble runs, so the temporal resolution is low. Only 87 members show readvance after deglaciation (62 Ronne, 13 Ross, and 12 both). In the best-fit member, the Ross deglaciation starts 2 thousand years earlier than the Ronne and the readvance happens in both basins (Figure 12e).

5.3. Interpreting Divide Stability

Based on the geologic evidence and paleo-ice-sheet model output interpreted in the prior section, Hercules Dome divide migration and rotation are *plausible* during ice-sheet deglaciation in the Holocene. Divide migration would have been driven by an offset in timing of deglaciation between Ross and Ronne. Divide rotation would have been driven by a more isolated dynamic change (e.g., activation of the subglacial valley to the northwest of HD Summit). However, the timing of those interpreted continental-scale changes (mid Holocene) are within the COF evolution timescales that we model in Section 4 (∼5 ka). If there were a broad dynamic change at Hercules Dome, we would expect it to be observable in the radar polarimetry measurements, but our results at HD Summit indicate consistent ice flow and relative divide stability.

Of course, with a COF timescale of approximately five thousand years we cannot make any direct claim about stability during the last glacial period or earlier. Instead, we argue our result lends to an interpretation of relative divide stability in a time of continental-scale ice-sheet deglaciation. Even with differential retreat between Ross and Ronne basins, we see no evidence of significant divide migration or reorientation which would present as girdle axes misaligned with the present-day dynamics. The HD Summit position is elevated on the Thiel Mountain Block (Figure 13). This thinner ice over higher bed topography is likely frozen (Fudge et al., 2022) and sediment poor, unlike the surrounding troughs and valleys (Hoffman, Holschuh, et al., 2023). Moreover, the subtle bed roughness, and especially the divide-coincident bedrock ridge, likely stabilize the position of the divide

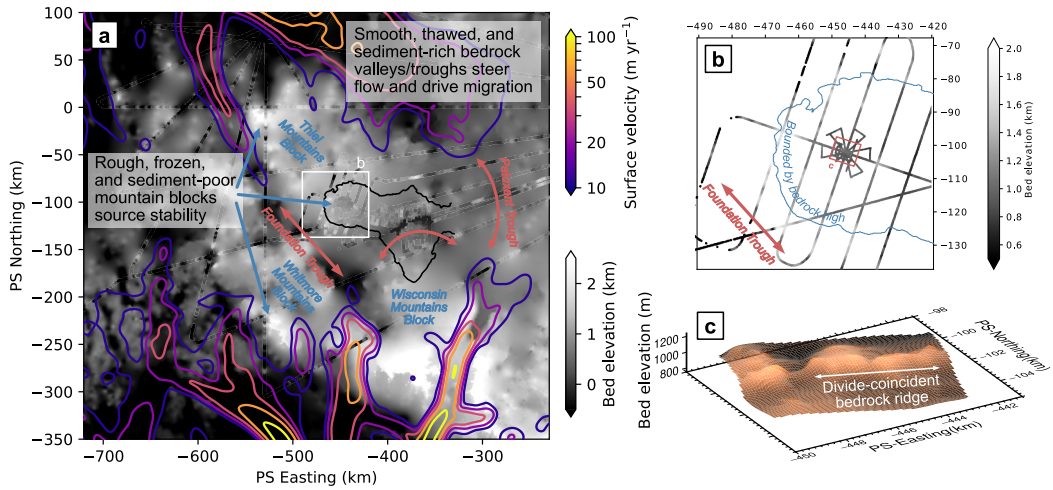

Figure 13. (a) An illustration of how bed topography drives ice flow in the bottleneck. The gridded bed elevation (Morlighem et al., 2020) and surface velocity contours (Mouginot et al., 2019) are as in Figure 2. The surface velocity is smoothed with a Gaussian filter and clipped at 10 m/yr in order to overlay on the bed topography. (b) Radar measurements of bed elevation at and near HD Summit. (c) Gridded bed elevation at the true summit (interpolated with a tension spline).

itself, with a smaller driving stress in the thinner ice over the ridge. Since the bed topography is relatively stable on the timescales considered here, we argue that interpretation of divide stability at the timescales considered here could be extended to earlier time periods.

If the divide dynamics are regionally stable, the remaining question is why we do not observe a prominent Raymond Arch as in some radar surveys elsewhere (Figure 1). First, the bed topography may obscure the stratigraphy. That is, the bedrock bump directly beneath the ice divide causes up-warping of layers which could be overprinted on the Raymond Arch making it difficult to interpret (Fudge et al., 2022; Figure 9).

Second, there are larger bedrock bumps ∼10 ice thicknesses from the dome summit in all directions, across the divide (Figure 1e) and along the divide (Figure S8 in Supporting Information S1). HD Summit therefore rests in an elevated basin, where the regional bed topography is lifted up on the Thiel Mountain Block, but closer to the true summit (within ∼2–5 ice thicknesses) the bed topography is below the rim of the regional bedrock basin. This bed geometry is potentially altering the ice flow characteristics from that of an idealized divide. Most observed Raymond Arches have been over a smooth bed with the one striking exception being at Adelaide Island (Martín, Gudmundsson, et al., 2009).

Third, as described in Section 5.2, divide stability depends not only on the ice flux downstream toward the ice shelves (considered here), but also on the input flux from precipitation (not considered here). Fudge et al. (2022) found that a good fit between their kinematic model and the observed stratigraphy required a change in divide position (and associated precipitation) before ∼six thousand years ago, but that only small changes (<1 ice thickness) were necessary. The stratigraphy is more sensitive to small changes in divide position while the COF considered here is more sensitive to the dynamic setting and shape of the dome itself over a broader spatial scale and longer timescale. We argue that a relatively small change in space or relatively brief change in time of the divide position could eliminate a Raymond Arch even when a Raymond Effect is observed in the vertical velocities (Gillet-Chaulet et al., 2011). Those small or brief changes may not reset the timescale for COF evolution.

The difference in divide dynamics between HD Summit (mostly unconfined, dome-like flow) and Belt (true divide with spreading in one direction) are evident in the polarimetry measurements. Since the true divide is only subject to changes in shear, it should not be expected to have a more prominent girdle at the divide itself than away from it. In fact, shear can strengthen the vertical girdle (Gerber et al., 2023; Smith et al., 2017). Therefore, changes in the divide position may not be measurable in the COF at Belt unless a well-developed Raymond Arch were present (Martín, Gudmundsson, et al., 2009). The unconfined, dome-like flow, on the other hand, includes a component of radial extension, so the strongest girdle should be expected where that component is minimized (at

21699011, 2025, 3, Downloaded from https://agupubs.onlinelibrary.wiley.com/doi/10.1029/2023JF007588 by Benjamin Hills - University Of Washington Lib , Wiley Online Library on [26/02/2025]. See the Terms and Conditions (https://onlinelibrary.wiley.com/terms-and-conditions) on Wiley Online Library for rules of use; OA articles are governed by the applicable Creative Commons License

21699011, 2025, 3, Downloaded from https://agupubs.onlinelibrary.wiley.com/doi/10.1029/2023JF007588 by Benjamin Hills - University Of Washington Lib , Wiley Online Library on [26/02/2025]. See the Terms and Conditions (https://onlinelibrary.wiley.com/terms-and-conditions) on Wiley Online Library for rules of use; OA articles are governed by the applicable Creative Commons License

the divide itself), as our results show. A similar divide-flow effect was observed in a transect of polarimetry acquisitions at Dome C (Ershadi et al., 2022).

Our polarimetry result from East Dome indicates consistent extension along the axis of the bedrock valley. This valley has therefore steered ice flow at least through deglaciation and continues to do so today. If the trough-like feature to the northwest of HD Summit had a similar effect on ice flow, it must pre-date the five thousand year period that contributed to fabric development we observe today. Otherwise, ice flow toward the valley would have formed a girdle oriented with it and that would be persistent today, which we do not observe in the closest polarimetry acquisitions. Instead, the measured girdle at that location is oriented approximately east–west, in line with the regional polarimetry results and interpreted north-south spreading at HD Summit.

6. Conclusions

In this study, we used geophysical techniques to measure present-day and infer historical ice-flow dynamics at Hercules Dome, assessing dynamic stability at a divide in the ice-sheet interior. We used our results to guide a model experiment on timescales for evolution of COF. Despite that Holocene ice-flow reconfiguration at Hercules Dome is plausible due to differential drawdown from the Ross and Ronne ice shelves, we found that the measured COF at Hercules Dome is in line with the present-day ice flow. The minimum COF evolution timescale under present-day strain rates is approximately five thousand years, so any significant change to the divide orientation or position during that time can be ruled out since the observed COF is consistent with present-day ice flow. As in prior work, we argue that the bed geometry largely controls ice flow at Hercules Dome, especially the Foundation and Patuxent troughs as well as one particularly large glacial valley running through East Dome (Hoffman, Holschuh, et al., 2023). The surveys presented here reveal that local bed topographic highs appear to control the position of HD Summit, and that this topography is too fine scale (<10 km) to be resolved in coarse continental-scale ice-sheet model simulations.

Of the Hercules Dome subregions discussed here, HD Summit is the most optimal as an ice-core drilling site. East Dome has thick ice, steep subglacial relief (which likely fosters heterogeneous melting), and possibly a more complicated flow history (Hoffman, Holschuh, et al., 2023). East Dome is therefore not likely to provide an undisturbed climate record far back in time. Belt and South Ridge are both extensional ridges, with South Ridge having some down-ridge (southward) flow component. While neither of these sites has any obvious criteria for exclusion in the way that East Dome does, they also do not stand out as optimal candidates for an ice-core drilling site. Both are underlain by a rough bed, but rather than a discrete bedrock ridge coincident with the surface divide, the underlying ridges and valleys span multiple ice thicknesses from the divide. Measured vertical velocities are approximately uniform in the case of South Ridge and seemingly influenced by bed-controlled shear at Belt. At HD Summit, the underlying bedrock ridge is narrow and directly underneath the surface divide, so it may be stabilizing ice flow. Measured vertical velocities demonstrate a progression from divide-like to flank-like flow, and measured girdle orientations are uniformly aligned with present-day ice flow across the HD Summit region. The measured girdle strength is greatest for sites within an ice thickness of the current divide. Our COF timescale modeling demonstrates that if the divide had significantly migrated or rotated at the summit within the last five thousand years, that signal would be preserved in the present-day COF and measurable in our polarimetry experiments (e.g., as girdle orientations misaligned from the present-day divide orientation). Instead, we argue that the divide position at HD Summit has remained roughly coincident with the bedrock ridge during the Holocene, despite significant retreat of the Antarctic ice sheet over the same period.

Conflict of Interest

The authors declare no conflicts of interest relevant to this study.

Data Availability Statement

All data sets presented in this article are publicly available through the United States Antarctic Program Data Center (USAP-DC) (posted under NSF award number 1744649 at https://www.usap-dc.org/view/project/p0010359). The ground-based profiling radar data used in this article were originally published by Hoffman, Christian, et al. (2023) with prior interpretations given in Fudge et al. (2022) and Hoffman, Holschuh,

et al. (2023). All the ApRES acquisitions, including both interferometry and polarimetry, are published together (Hills et al., 2023).

Software used for processing of impulse radar data sets is made available by Lilien et al. (2020). MCoRDS profiles were generated using software from Open Polar Radar (2024) generated with support from the University of Kansas, NASA grants 80NSSC20K1242 and 80NSSC21K0753, and NSF grants OPP-2027615, OPP-2019719, OPP-1739003, IIS-1838230, RISE-2126503, RISE-2127606, and RISE-2126468. The spectral fabric model was originally published by Rathmann et al. (2021).

We also take advantage of several public data products, including:

- Ground-based radar from the ITASE traverse (Welch & Jacobel, 2003) with data made public on the USAP-DC (Hoffman, Christianson, et al., 2023).
- Airborne radar supported by the Center for Oldest Ice Exploration (pers. comm. Duncan Young), published on the CReSIS server (CReSIS, 2024).
- Airborne radar from the British Antarctic Survey PolarGap project, published on their data portal (Ferraccioli et al., 2021).
- Paleo ice-sheet model output from Albrecht et al. (2020b), published on PANGAEA (Albrecht, 2019).
- Geologic exposure ages cited throughout and published online at Ice-D Antarctica (Balco, 2020).

Acknowledgments
We thank the editor, Olga Sergienko, as well as Nicholas Rathmann and two more anonymous reviewers. BHH processed the data, conceptualized the model experiments, and wrote the original manuscript. KC, NDH, and AOH provided significant feedback to radar processing and interpretation. KC, EJS, and TJF proposed the research. All authors participated in fieldwork, survey design, and contributed to writing. We want to acknowledge additional contributions from the numerous teams who made this work possible. We would like to thank the additional members to the field teams who made measurements on the ground at Hercules Dome, including: 2018-'19 season) Geoff Schellens; 2019-'20 season) Vito Cicola, John Christian, Gemma O'Connor, and Shannon Wilson; 2021-'22 season) Robert Caldwell and Erika Schreiber; 2022-'23 season) Michael Kingsbury. We thank the airborne geophysics team from the Center for Oldest Ice Exploration for their airborne survey of Hercules Dome in January 2023. We thank the New York Air National Guard and Kenn Borek Air for transportation support in Antarctica. We thank the US Antarctic Support Contract for logistical support, with special thanks to Jenny Cunningham, Bija Sass, Jennifer Blum, and Sheryl Seagraves. This research was supported by NSF Grants 1744649 and 1841844. BHH was supported in part by NSF Grant 2317927. NDH was supported in part by NASA Grant 80NSSC21K0753.

References

Ackert, R. P., Mukhopadhyay, S., Pollard, D., DeConto, R. M., Putnam, A. E., & Borns, H. W. (2011). West Antarctic Ice Sheet elevations in the Ohio Range: Geologic constraints and ice sheet modeling prior to the last highstand. *Earth and Planetary Science Letters*, *307*(1–2), 83–93. https://doi.org/10.1016/j.epsl.2011.04.015

Albrecht, T. (2019). PISM parameter ensemble analysis of Antarctic Ice Sheet glacial cycle simulations [Dataset]. *PANGAEA*. https://doi.org/10.1594/PANGAEA.909728

Albrecht, T., Winkelmann, R., & Levermann, A. (2020a). Glacial-cycle simulations of the Antarctic Ice Sheet with the Parallel Ice Sheet Model (PISM)-Part 1: Boundary conditions and climatic forcing. *The Cryosphere*, *14*(2), 599–632. https://doi.org/10.5194/tc-14-599-2020

Albrecht, T., Winkelmann, R., & Levermann, A. (2020b). Glacial-cycle simulations of the Antarctic Ice Sheet with the Parallel Ice Sheet Model (PISM)-Part 2: Parameter ensemble analysis. *The Cryosphere*, *14*(2), 633–656. https://doi.org/10.5194/tc-14-633-2020

Anderson, J. B., Conway, H., Bart, P. J., Witus, A. E., Greenwood, S. L., McKay, R. M., et al. (2014). Ross Sea paleo-ice sheet drainage and deglacial history during and since the LGM. *Quaternary Science Reviews*, *100*, 31–54. https://doi.org/10.1016/j.quascirev.2013.08.020

Balco, G. (2020). Technical note: A prototype transparent-middle-layer data management and analysis infrastructure for cosmogenic-nuclide exposure dating. *Geochronology*, *2*(2), 169–175. https://doi.org/10.5194/gchron-2-169-2020

Balco, G., Todd, C., Huybers, K., Campbell, S., Vermeulen, M., Hegland, M., et al. (2016). Cosmogenic-nuclide exposure ages from the Pensacola Mountains adjacent to the foundation ice stream, Antarctica. *American Journal of Science*, *316*(6), 542–577. https://doi.org/10.2475/06.2016.02

Brennan, P. V., Lok, L. B., Nicholls, K., & Corr, H. (2014). Phase-sensitive FMCW radar system for high-precision antarctic ice shelf profile monitoring. *IET Radar, Sonar & Navigation*, *8*(7), 776–786. https://doi.org/10.1049/iet-rsn.2013.0053

Brisbourne, A. M., Martín, C., Smith, A. M., Baird, A. F., Kendall, J. M., & Kingslake, J. (2019). Constraining recent ice flow history at Korff ice rise, West Antarctica, using radar and seismic measurements of ice fabric. *Journal of Geophysical Research: Earth Surface*, *124*(1), 175–194. https://doi.org/10.1029/2018JF004776

Budd, W., & Jacka, T. (1989). A review of ice rheology for ice sheet modelling. *Cold Regions Science and Technology*, *16*(2), 107–144. https://doi.org/10.1016/0165-232x(89)90014-1

Christianson, K., Jacobel, R. W., Horgan, H. J., Alley, R. B., Anandakrishnan, S., Holland, D. M., & Dallasanta, K. J. (2016). Basal conditions at the grounding zone of Whillans Ice Stream, West Antarctica, from ice-penetrating radar. *Journal of Geophysical Research: Earth Surface*, *121*(11), 1954–1983. https://doi.org/10.1002/2015JF003806

Conway, H., Catania, G., Raymond, C. F., Gades, A. M., Scambos, T. A., & Engelhardt, H. (2002). Switch of flow direction in an antarctic ice stream. *Nature*, *419*(6906), 465–467. https://doi.org/10.1038/nature01081

Conway, H., Hall, B. L., Denton, G. H., Gades, A. M., & Waddington, E. D. (1999). Past and future grounding-line retreat of the West Antarctic Ice Sheet. *Science*, *286*(5438), 280–283. https://doi.org/10.1126/science.286.5438.280

CReSIS. (2024). MCoRDS data [Dataset]. http://data.cresis.ku.edu/

DeConto, R. M., & Pollard, D. (2016). Contribution of Antarctica to past and future sea-level rise. *Nature*, *531*(7596), 591–597. https://doi.org/10.1038/nature17145

Dütsch, M., Steig, E. J., Blossey, P. N., & Pauling, A. G. (2023). Response of water isotopes in precipitation to a collapse of the West Antarctic Ice Sheet in high-resolution simulations with the Weather Research and Forecasting Model. *Journal of Climate*, *36*(16), 5417–5430. https://doi.org/10.1175/JCLI

Ershadi, M. R., Drews, R., Martín, C., Eisen, O., Ritz, C., Corr, H., et al. (2022). Polarimetric radar reveals the spatial distribution of ice fabric at domes and divides in East Antarctica. *The Cryosphere*, *16*(5), 1719–1739. https://doi.org/10.5194/tc-16-1719-2022

Ferraccioli, F., Forsberg, R., Matsuoka, K., Olesen, A., Jordan, T., Corr, H., et al. (2021). Processed airborne radio-echo sounding data from the POLARGAP survey covering the South Pole, and Foundation and Recovery Glaciers, East Antarctica (2015/2016) (Version 1.0) [Dataset]. *NERC EDS UK Polar Data Centre*. https://doi.org/10.5285/e8a29fa7-a245-4a04-8b56-098defa134b9

Fudge, T. J., Hills, B. H., Horlings, A. N., Holschuh, N., Christian, J. E., Davidge, L., et al. (2022). A site for deep ice coring at West Hercules Dome: Results from ground-based geophysics and modeling. *Journal of Glaciology*, *69*(275), 1–13. https://doi.org/10.1017/jog.2022.80

Fujita, S., Maeno, H., & Matsuoka, K. (2006). Radio-wave depolarization and scattering within ice sheets: A matrix-based model to link radar and ice-core measurements and its application. *Journal of Glaciology*, *52*(178), 407–424. https://doi.org/10.3189/172756506781828548

21699011, 2025, 3, Downloaded from https://agupubs.onlinelibrary.wiley.com/doi/10.1029/2023JF007588 by Benjamin Hills - University Of Washington Lib , Wiley Online Library on [26/02/2025]. See the Terms and Conditions (https://onlinelibrary.wiley.com/terms-and-conditions) on Wiley Online Library for rules of use; OA articles are governed by the applicable Creative Commons License

Gades, A. M., Raymond, C. F., Conway, H., & Jacobel, R. W. (2000). Bed properties of Siple Dome and adjacent ice streams, West Antarctica, inferred from radio-echo sounding measurements. *Journal of Glaciology*, *46*(152), 88–94. https://doi.org/10.3189/172756500781833467

Gerber, T. A., Lilien, D., Rathmann, N., Franke, S., Young, T. J., Valero-Delgado, F., et al. (2023). Crystal fabric anisotropy causes directional hardening of the Northeast Greenland Ice Stream. *Nature Communications*, *14*(1), 2653. https://doi.org/10.1038/s41467-023-38139-8

Gillet-Chaulet, F., Hindmarsh, R. C., Corr, H. F., King, E. C., & Jenkins, A. (2011). In-situ quantification of ice rheology and direct measurement of the Raymond Effect at Summit, Greenland using a phase-sensitive radar. *Geophysical Research Letters*, *38*(24), 1–6. https://doi.org/10.1029/2011GL049843

Golledge, N. R., Fogwill, C. J., Mackintosh, A. N., & Buckley, K. M. (2012). Dynamics of the last glacial maximum Antarctic ice-sheet and its response to ocean forcing. *Proceedings of the National Academy of Sciences of the United States of America*, *109*(40), 16052–16056. https://doi.org/10.1073/pnas.1205385109

Haran, T., Klinger, M., Bohlander, J., Fahnestock, M., Painter, T., & Scambos, T. A. (2018). MEaSUREs MODIS Mosaic of Antarctica 2013-2014 (MOA2014) image map [Dataset]. *NASA National Snow and Ice Data Center Distributed Active Archive Center*. https://doi.org/10.5067/RNF17BP824UM

Hills, B. H., Christianson, K., Hoffman, A. O., Fudge, T. J., Holschuh, N., Kahle, E. C., et al. (2022). Geophysics and thermodynamics at South Pole Lake indicate stability and a regionally thawed bed. *Geophysical Research Letters*, *49*(2), 1–10. https://doi.org/10.1029/2021GL096218

Hills, B. H., Holschuh, A., Nicholas, H., Fudge, T. J., Horlings, A., Erwin, E., et al. (2023). Hercules dome ApRES data [Dataset]. *U.S. Antarctic Program Data Center*. https://doi.org/10.15784/601739

Hoffman, A. O., Christian, J., Christianson, K., Hills, B., Holschuh, N., Horlings, A., & O'Connor, G. (2023). Hercules dome high-frequency impulse ice-penetrating radar data [Dataset]. *U.S. Antarctic Program Data Center*. https://doi.org/10.15784/601710

Hoffman, A. O., Christianson, K., Jacobel, R., & Welch, B. (2023). ITASE impulse radar Hercules dome to South Pole [Dataset]. *U.S. Antarctic Program Data Center*. https://doi.org/10.15784/601712

Hoffman, A. O., Holschuh, N., Mueller, M., Paden, J., Muto, A., Ariho, G., et al. (2023). Scars of tectonism promote ice-sheet nucleation from Hercules Dome into West Antarctica. *Nature Geoscience*, *16*(11), 1005–1013. https://doi.org/10.1038/s41561-023-01265-5

Howat, I. M., Porter, C., Smith, B. E., Noh, M.-J., & Morin, P. (2019). The reference elevation model of Antarctica. *The Cryosphere*, 1–16. https://doi.org/10.5194/tc-2018-240

Huybers, K., Roe, G., & Conway, H. (2017). Basal topographic controls on the stability of the West Antarctic ice sheet: Lessons from Foundation Ice Stream. *Annals of Glaciology*, *58*(75), 193–198. https://doi.org/10.1017/aog.2017.9

Jacobel, R. W., Welch, B. C., Steig, E. J., & Schneider, D. P. (2005). Glaciological and climatic significance of Hercules Dome, Antarctica: An optimal site for deep ice core drilling. *Journal of Geophysical Research*, *110*(1), 1–9. https://doi.org/10.1029/2004JF000188

Johnson, J. S., Venturelli, R. A., Balco, G., Allen, C. S., Braddock, S., Campbell, S., et al. (2022). Review article: Existing and potential evidence for Holocene grounding line retreat and readvance in Antarctica. *The Cryosphere*, *16*(5), 1543–1562. https://doi.org/10.5194/tc-16-1543-2022

Jones, R. S., Johnson, J. S., Lin, Y., Mackintosh, A. N., Sefton, J. P., Smith, J. A., et al. (2022). Stability of the Antarctic Ice Sheet during the pre-industrial Holocene. *Nature Reviews Earth & Environment*, *3*(8), 500–515. https://doi.org/10.1038/s43017-022-00309-5

Jordan, T. M., Martín, C., Brisbourne, A. M., Schroeder, D. M., & Smith, A. M. (2022). Radar characterization of ice crystal orientation fabric and anisotropic viscosity within an Antarctic Ice Stream. *Journal of Geophysical Research: Earth Surface*, *127*(6), 1–24. https://doi.org/10.1029/2022JF006673

Jordan, T. M., Schroeder, D. M., Castelletti, D., Li, J., & Dall, J. (2019). A polarimetric coherence method to determine ice crystal orientation fabric from radar sounding: Application to the NEEM ice core region. *IEEE Transactions on Geoscience and Remote Sensing*, *57*(11), 8641–8657. https://doi.org/10.1109/TGRS.2019.2921980

Kingslake, J., Hindmarsh, R. C. A., Aðalgeirsdóttir, G., Conway, H., Corr, H. F. J., Gillet-Chaulet, F., et al. (2014). Full-depth englacial vertical ice sheet velocities measured using phase-sensitive radar. *Journal of Geophysical Research F: Earth Surface*, *119*(12), 2604–2618. https://doi.org/10.1002/2014JF003275

Kingslake, J., Martín, C., Arthern, R. J., Corr, H. F., & King, E. C. (2016). Ice-flow reorganization in West Antarctica 2.5 kyr ago dated using radar-derived englacial flow velocities. *Geophysical Research Letters*, *43*(17), 9103–9112. https://doi.org/10.1002/2016GL070278

Kingslake, J., Scherer, R. P., Albrecht, T., Coenen, J., Powell, R. D., Reese, R., et al. (2018). Extensive retreat and re-advance of the West Antarctic Ice Sheet during the Holocene. *Nature*, *558*(7710), 430–434. https://doi.org/10.1038/s41586-018-0208-x

Lau, S. C., Wilson, N. G., Golledge, N. R., Naish, T. R., Watts, P. C., Silva, C. N., et al. (2023). Genomic evidence for West Antarctic Ice Sheet collapse during the last interglacial. *Science*, *382*(6677), 1384–1390. https://doi.org/10.1126/science.ade0664

Lilien, D. A., Hills, B. H., Driscol, J., Jacobel, R., & Christianson, K. (2020). ImpDAR: An open-source impulse radar processor. *Annals of Glaciology*, *61*(81), 114–123. https://doi.org/10.1017/aog.2020.44

Lilien, D. A., Rathmann, N. M., Hvidberg, C. S., Grinsted, A., Ershadi, M. R., Drews, R., & Dahl-Jensen, D. (2023). Simulating higher-order fabric structure in a coupled, anisotropic ice-flow model: Application to Dome C. *Journal of Glaciology*, 1–20. https://doi.org/10.1017/jog.2023.78

Lliboutry, L. (1979). A critical review of analytical approximate solutions for steady state velocities and temperatures in cold ice-sheets. *Gletscherkd. Glazialgeol.*, *15*(2), 135–148.

Martín, C., Gudmundsson, G. H., Pritchard, H. D., & Gagliardini, O. (2009). On the effects of anisotropic rheology on ice flow, internal structure, and the age-depth relationship at ice divides. *Journal of Geophysical Research*, *114*(4), 1–18. https://doi.org/10.1029/2008JF001204

Martín, C., Hindmarsh, R. C., & Navarro, F. J. (2009). On the effects of divide migration, along-ridge flow, and basal sliding on isochrones near an ice divide. *Journal of Geophysical Research*, *114*(2), 1–17. https://doi.org/10.1029/2008JF001025

Matsuoka, T., Fujita, S., Morishima, S., & Mae, S. (1997). Precise measurement of dielectric anisotropy in ice Ih at 39 GHz. *Journal of Applied Physics*, *81*(5), 2344–2348. https://doi.org/10.1063/1.364238

Mitrovica, J. X., Tamisiea, M. E., Davis, J. L., & Milne, G. A. (2001). Recent mass balance of polar ice sheets inferred from patterns of global sea-level change. *Nature*, *409*(February), 4–7. https://doi.org/10.1038/35059054

Morlighem, M., Rignot, E., Binder, T., Blankenship, D., Drews, R., Eagles, G., et al. (2020). Deep glacial troughs and stabilizing ridges unveiled beneath the margins of the Antarctic ice sheet. *Nature Geoscience*, *13*(2), 132–137. https://doi.org/10.1038/s41561-019-0510-8

Mouginot, J., Rignot, E., & Scheuchl, B. (2019). Continent-wide, interferometric SAR phase, mapping of Antarctic ice velocity. *Geophysical Research Letters*, *46*(16), 9710–9718. https://doi.org/10.1029/2019GL083826

Nereson, N. A., Raymond, G. F., Waddington, E. D., & Jacobel, R. W. (1998). Migration of the Siple Dome ice divide, West Antarctica. *Journal of Glaciology*, *44*(148), 643–652. https://doi.org/10.1017/S0022143000002148

Neumann, T. A., Conways, H., Price, S. F., Waddington, E. D., Catania, G. A., & Morse, D. L. (2008). Holocene accumulation and ice sheet dynamics in central West Antarctica. *Journal of Geophysical Research*, *113*(2), 1–9. https://doi.org/10.1029/2007JF000764

21699011, 2025, 3, Downloaded from https://agupubs.onlinelibrary.wiley.com/doi/10.1029/2023JF007588 by Benjamin Hills - University Of Washington Lib , Wiley Online Library on [26/02/2025]. See the Terms and Conditions (https://onlinelibrary.wiley.com/terms-and-conditions) on Wiley Online Library for rules of use; OA articles are governed by the applicable Creative Commons License

Nicholls, K. W., Corr, H. F., Stewart, C. L., Lok, L. B., Brennan, P. V., & Vaughan, D. G. (2015). Instruments and methods: A ground-based radar for measuring vertical strain rates and time-varying basal melt rates in ice sheets and shelves. *Journal of Glaciology*, *61*(230), 1079–1087. https://doi.org/10.3189/2015JoG15J073

Nichols, K. A., Goehring, B. M., Balco, G., Johnson, J. S., Hein, A. S., & Todd, C. (2019). New Last Glacial Maximum ice thickness constraints for the Weddell Sea Embayment, Antarctica. *The Cryosphere*, *13*(11), 2935–2951. https://doi.org/10.5194/tc-13-2935-2019

Open Polar Radar. (2024). Opr (version 3.0.1) [Software]. Retrieved from https://gitlab.com/openpolarradar/opr/doi:10.5281/zenodo.5683959

Pettit, E. C., Jacobson, H. P., & Waddington, E. D. (2003). Effects of basal sliding on isochrones and flow near an ice divide. *Annals of Glaciology*, *37*, 370–376. https://doi.org/10.1029/2008JF001025

Pettit, E. C., & Waddington, E. (2003). Ice flow at low deviatoric stress. *Journal of Glaciology*, *49*(166), 359–369. https://doi.org/10.1002/9780470750636.ch58

Placidi, L., Greve, R., Seddik, H., & Faria, S. H. (2010). Continuum-mechanical, Anisotropic Flow model for polar ice masses, based on an anisotropic Flow Enhancement factor. *Continuum Mechanics and Thermodynamics*, *22*(3), 221–237. https://doi.org/10.1007/s00161-009-0126-0

Rathmann, N. M., Hvidberg, C. S., Grinsted, A., Lilien, D. A., & Dahl-Jensen, D. (2021). Effect of an orientation-dependent non-linear grain fluidity on bulk directional enhancement factors. *Journal of Glaciology*, *67*(263), 569–575. https://doi.org/10.1017/jog.2020.117

Rathmann, N. M., & Lilien, D. A. (2021). Inferred basal friction and mass flux affected by crystal-orientation fabrics. *Journal of Glaciology*, *68*(268), 236–252. https://doi.org/10.1017/jog.2021.88

Rathmann, N. M., Lilien, D. A., Grinsted, A., Gerber, T. A., Young, T. J., & Dahl-Jensen, D. (2022). On the limitations of using polarimetric radar sounding to infer the crystal orientation fabric of ice masses. *Geophysical Research Letters*, *49*(1), 1–11. https://doi.org/10.1029/2021GL096244

Raymond, C. F. (1983). Deformation in the vicinity of ice divides. *Journal of Glaciology*, *29*(103), 357–373. https://doi.org/10.3189/S0022143000030288

Richards, D. H., Pegler, S. S., Piazolo, S., & Harlen, O. G. (2021). The evolution of ice fabrics: A continuum modelling approach validated against laboratory experiments. *Earth and Planetary Science Letters*, *556*, 116718. https://doi.org/10.1016/j.epsl.2020.116718

Savage, M. S. (1999). Seismic anisotropy and mantle deformation: What have we learned from shear wave splitting? *Reviews of Geophysics*, *37*(1), 65–106. https://doi.org/10.1029/98RG02075

Siegert, M., Ross, N., Corr, H., Kingslake, J., & Hindmarsh, R. (2013). Late Holocene ice-flow reconfiguration in the Weddell Sea sector of West Antarctica. *Quaternary Science Reviews*, *78*, 98–107. https://doi.org/10.1016/j.quascirev.2013.08.003

Smith, E. C., Baird, A. F., Kendall, J. M., Martín, C., White, R. S., Brisbourne, A. M., & Smith, A. M. (2017). Ice fabric in an Antarctic ice stream interpreted from seismic anisotropy. *Geophysical Research Letters*, *44*(8), 3710–3718. https://doi.org/10.1002/2016GL072093

Spratt, R. M., & Lisiecki, L. E. (2016). A Late Pleistocene sea level stack. *Climate of the Past*, *12*(4), 1079–1092. https://doi.org/10.5194/cp-12-1079-2016

Steig, E. J., Huybers, K., Singh, H. A., Steiger, N. J., Ding, Q., Frierson, D. M. W., et al. (2015). Influence of West Antarctic Ice Sheet collapse on Antarctic surface climate. *Geophysical Research Letters*, *42*(12), 4862–4868. https://doi.org/10.1002/2015GL063861.Abstract

Steig, E. J., Mayewski, P. A., Dixon, D. A., Kaspari, S. D., Frey, M. M., Schneider, D. P., et al. (2005). High-resolution ice cores from US ITASE (West Antarctica): Development and validation of chronologies and determination of precision and accuracy. *Annals of Glaciology*, *41*, 77–84. https://doi.org/10.3189/172756405781813311

Stone, J., Balco, G., Sugden, D., Caffee, M., Sass, L. III, Cowdery, S., & Siddoway, C. (2003). Holocene Deglaciation of Marie Byrd Land, West Antarctica. *Science*, *299*(January), 99–102. https://doi.org/10.1126/science.1077998

Tétreault, P., Kouba, J., Héroux, P., & Legree, P. (2005). CSRS-PPP: An internet service for GPS user access to the Canadian spatial reference frame. *Geomatica*, *59*(1), 17–28. https://doi.org/10.5623/geomat-2005-0004

Todd, C., Stone, J., Conway, H., Hall, B., & Bromley, G. (2010). Late Quaternary evolution of Reedy Glacier, Antarctica. *Quaternary Science Reviews*, *29*(11–12), 1328–1341. https://doi.org/10.1016/j.quascirev.2010.02.001

Vaughan, D. G., Corr, H. F., Doake, C. S., & Waddington, E. D. (1999). Distortion of isochronous layers in ice revealed by ground-penetrating radar. *Nature*, *398*(6725), 323–326. https://doi.org/10.1038/18653

Venturelli, R. A., Boehman, B., Davis, C., Hawkings, J. R., Johnston, S. E., Gustafson, C. D., et al. (2023). Constraints on the timing and extent of deglacial grounding line retreat in West Antarctica. *AGU Advances*, *4*(2), 1–15. https://doi.org/10.1029/2022AV000846

Venturelli, R. A., Siegfried, M. R., Roush, K. A., Li, W., Burnett, J., Zook, R., et al. (2020). Mid-holocene grounding line retreat and readvance at Whillans ice stream, West Antarctica. *Geophysical Research Letters*, *47*(15). https://doi.org/10.1029/2020GL088476

Welch, B. C., & Jacobel, R. W. (2003). Analysis of deep-penetrating radar surveys of West Antarctica, US-ITASE 2001. *Geophysical Research Letters*, *30*(8), 1–4. https://doi.org/10.1029/2003GL017210

Whitehouse, P. L., Bentley, M. J., Vieli, A., Jamieson, S. S., Hein, A. S., & Sugden, D. E. (2017). Controls on last glacial maximum ice extent in the Weddell sea embayment, Antarctica. *Journal of Geophysical Research: Earth Surface*, *122*(1), 371–397. https://doi.org/10.1002/2016jf004121

Winter, K., Ross, N., Ferraccioli, F., Jordan, T. A., Corr, H. F., Forsberg, R., et al. (2018). Topographic steering of enhanced ice flow at the bottleneck between East and West Antarctica. *Geophysical Research Letters*, *45*(10), 4899–4907. https://doi.org/10.1029/2018GL077504

Young, T., Martín, C., Christoffersen, P., Schroeder, D., Tulaczyk, S. M., & Dawson, E. J. (2021). Rapid and accurate polarimetric radar measurements of ice crystal fabric orientation at the Western Antarctic Ice Sheet (WAIS) Divide ice core site. *The Cryosphere*, *15*(8), 4117–4133. https://doi.org/10.5194/tc-15-4117-2021

Zeising, O., Gerber, T. A., Eisen, O., Ershadi, M. R., Stoll, N., Weikusat, I., & Humbert, A. (2023). Improved estimation of the bulk ice crystal fabric asymmetry from polarimetric phase co-registration. *The Cryosphere*, *17*(3), 1097–1105. https://doi.org/10.5194/tc-17-1097-2023

References From the Supporting Information

Alley, R. B., Gow, A. J., & Meese, D. A. (1995). Mapping c-axis fabrics to study physical processes in ice. *Journal of Glaciology*, *41*(137), 197–203. https://doi.org/10.1017/S0022143000017895

Durand, G. (2004). *Microstructure, recristallisation et déformation des glaces polaires de la carotte epica, dôme concordia, antarctique* (Unpublished doctoral dissertation). Université Joseph-Fourier-Grenoble I.

Glen, J. W. (1955). The creep of polycrystalline ice. *Proceedings of the Royal Society of London: Mathematical, Physical and Engineering Sciences*, *228*(1175), 519–538. https://doi.org/10.1098/rspa.1955.0066

21699011, 2025, 3, Downloaded from https://agupubs.onlinelibrary.wiley.com/doi/10.1029/2023JF007588 by Benjamin Hills - University Of Washington Lib , Wiley Online Library on [26/02/2025]. See the Terms and Conditions (https://onlinelibrary.wiley.com/terms-and-conditions) on Wiley Online Library for rules of use; OA articles are governed by the applicable Creative Commons License

Gödert, G., & Hutter, K. (1998). Induced anisotropy in large ice shields: Theory and its homogenization. *Continuum Mechanics and Thermodynamics*, *10*(5), 293–318. https://doi.org/10.1007/s001610050095

Richards, D. H., Pegler, S. S., Piazolo, S., Stoll, N., & Weikusat, I. (2023). Bridging the gap between experimental and natural fabrics: Modeling ice stream fabric evolution and its comparison with ice-core data. *Journal of Geophysical Research: Solid Earth*, *128*(11), 1–18. https://doi.org/10.1029/2023JB027245

Svendsen, B., & Hutter, K. (1996). A continuum approach for modelling induced anisotropy in glaciers and ice sheets. *Annals of Glaciology*, *23*, 262–269. https://doi.org/10.1017/s0260305500013525

21699011, 2025, 3, Downloaded from https://agupubs.onlinelibrary.wiley.com/doi/10.1029/2023JF007588 by Benjamin Hills - University Of Washington Lib , Wiley Online Library on [26/02/2025]. See the Terms and Conditions (https://onlinelibrary.wiley.com/terms-and-conditions) on Wiley Online Library for rules of use; OA articles are governed by the applicable Creative Commons License